



Bilayered nano-hetero-structured n/n junction thin-film electrodes, $\text{WO}_3/\text{Yb-Mo-BiVO}_4$, for efficient photoelectrochemical water splitting

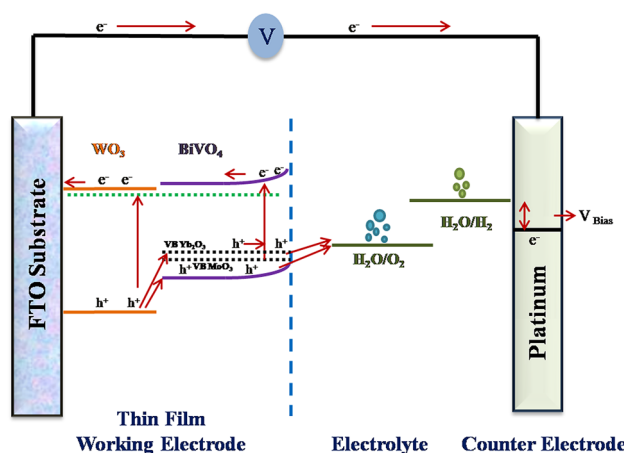
Divya¹ · Jyoti Prakash^{2,3} · Sakshi Saxena¹ · Pushpendra Kumar⁴ · Sahab Dass¹ · Arunachala Mada Kannan² · Rohit Shrivastav¹

Received: 11 July 2021 / Accepted: 24 November 2021 / Published online: 15 January 2022
© The Author(s), under exclusive licence to Springer Nature B.V. 2021

Abstract

Significant advancement in photoelectrochemical water splitting current is observed using uniquely evolved n/n junction bilayered nano-hetero-structured thin films, $\text{WO}_3/\text{Yb-Mo-BiVO}_4$, as photoanode. Films, synthesized over F:SnO₂ glass substrates were characterized by UV–Visible spectroscopy, X-ray diffractometry, atomic force microscopy, field-emission scanning electron microscopy, energy-dispersive X-ray spectroscopy, transmission electron microscopy and X-ray photoelectron spectroscopy. Using thin films (2% Mo and 4% Yb incorporation) as working electrode in PEC cell, in conjunction with platinum counter electrode, saturated calomel reference electrode, aqueous solution (200 cm³) of K_2HPO_4 (1.0 M, pH 8.7, temperature 31 ± 3.6 °C) and 150 W Xenon Arc lamp for illumination, ~227–950% increase in I_{ph} is recorded against monolayered pristine films of WO_3 and BiVO_4 . Marked rise in photoelectrochemical cell photocurrent is attributable to expanded absorption of light, coupled with internal electric field in Yb–Mo-incorporated n/n hetero-junction films, reduced electrical resistivity and optimally raised surface roughness that favoured the separation and transfer of photogenerated charge carriers across electrode/electrolyte interface.

Graphical Abstract



Keywords $\text{WO}_3/\text{Yb-Mo-BiVO}_4$ · Bilayered thin films · Nano-hetero-structure · Photoelectrochemical water splitting · Hydrogen

✉ Rohit Shrivastav
rohishrivastav_dei@yahoo.co.in

Extended author information available on the last page of the article

1 Introduction

Optimization of electrochemical processes lies at the core in the on-going research pursuits for efficient photoelectrochemical (PEC) cell to produce environmentally benign and renewable chemical fuel, viz. hydrogen, using abundantly available solar energy and water [1]. Solar light-induced photosplitting of water offers acquiescent and strategic roadmap for small and medium-scale hydrogen generation, paving the way to a new world ‘Hydrogen Economy’ [2]. However, efficiency of energy conversion in PEC cell pivots critically on material characteristics of semiconductor photoelectrode, which is an important component of cell. Photoelectrode in PEC cell performs dual role of generating electron–hole pairs on absorption of light and facilitating water-splitting electrochemical redox reactions [3]. For efficient absorption of solar light and to meet thermodynamic and electrochemical criteria for splitting of water molecule in PEC cell, band gap energy (E_g) of semiconductor used to fabricate photoelectrode must fall in the range 1.8–2.0 eV. Whilst semiconductors with too high band gap are unable to absorb bulk of solar energy present in visible region, those with too low band gap fail to generate the required potential to drive water-splitting reaction spontaneously [4]. Electrochemical stability, availability and cost are other important criteria to judge the suitability of semiconductor for this purpose [5, 6]. Metal oxide semiconductors are the most widely investigated and continue to hold interest for above application, as many of them are earth abundant, non-toxic and chemically stable [7, 8].

With ~12% absorption of solar spectrum (indirect band gap energy ~2.5–2.9 eV), WO_3 is n-type semiconductor and promising material, like TiO_2 and $\alpha\text{-Fe}_2\text{O}_3$, for PEC cell applications. Hole diffusion length in WO_3 is moderate (~150 nm), against very low in $\alpha\text{-Fe}_2\text{O}_3$ (2.4 nm) [9]. With oxygen vacancies in the structure, which serve as shallow donors, WO_3 exhibits reasonably good electron transport

(~12 $\text{cm}^2 \text{V}^{-1} \text{s}^{-1}$), higher than TiO_2 (~0.3 $\text{cm}^2 \text{V}^{-1} \text{s}^{-1}$) [10]. Further, deep valence band maxima of WO_3 favour oxygen production [11]. Still, WO_3 electrodes suffer with sluggish movement of holes and delayed charge transfer at electrode–electrolyte interface, which accounts for high recombination losses [12]. Impurity doping in WO_3 , studied by many workers to enhance its light absorption and PEC performance, had yielded mixed results [13, 14]. WO_3 can be easily grown as film where method of synthesis is critical to impart properties at nanoscale viz. effective surface area, crystallinity, defects and porosity, which are critical in the role of films as photoelectrode in PEC cell [15].

With conduction band edge placed favourably for H_2 evolution, BiVO_4 is another promising photoanode material [16, 17]. It exists in three polymorphic forms: monoclinic scheelite, tetragonal scheelite and tetragonal zircon structures, with monoclinic scheelite being thermodynamically most stable [16]. With a direct band gap of ~2.4 eV, conduction band minima and valence band maxima in BiVO_4 arise from hybridization of O 2p and Bi 6s orbitals with V 3d orbitals. With distortion of Bi^{3+} lone pair of electron, the scheelite monoclinic phase exhibits higher photocatalytic activity [18]. Few drawbacks that BiVO_4 encounters as photoelectrode are high rate of charge recombination, low carrier mobility and sluggish reaction kinetics. Various strategies have been employed in the past to alleviate these limitations, which include metal doping to improve conductivity, controlling morphologies, use of co-catalyst and creation of nano-hetero-structures [19].

Current estimates suggest that commercial success of solar light-assisted renewable hydrogen generation by PEC water splitting is attainable only if the energy conversion efficiency exceeds the minimum threshold limit (~10%), which at present is hovering around 1–3%. Material systems that have yielded high efficiency in few earlier investigations are either unstable or too expensive [20]. Faced with such challenges, studies are motivated in recent years to design

Table 1 Density (d) and thickness (t) data for thin-film samples

Sample	Description		Sample acronym	d (g cm^{-3})	t (nm)
<i>Mono-layered films</i>					
Pristine WO_3	WO_3		WP	2.03	410
Pristine BiVO_4	BiVO_4		BP	3.08	260
Mo-Yb- BiVO_4	2% Mo-1% Yb-incorporated BiVO_4		B1	3.00	294
	2% Mo-2% Yb-incorporated BiVO_4		B2	2.89	302
	2% Mo-4% Yb-incorporated BiVO_4		B4	2.68	331
	2% Mo-6% Yb-incorporated BiVO_4		B6	2.41	345
<i>Bilayered films</i>					
	<i>Under-layer</i>	<i>Over-layer</i>			
BNH Pristine	WO_3	BiVO_4	WB	2.20	640
Mo-Yb-BNH	WO_3	2% Mo-4% Yb-incorporated BiVO_4	WB4	2.01	730

and fabricate new generation photoelectrodes, represented by bilayered nano-hetero-structured (BNH) thin films of semiconductors. Although, the idea of semiconductor hetero-structuring was proposed much earlier [21], its use to evolve effective photoelectrode/photocatalyst for reactions of importance has gained significance only in last two decades [22–25]. BNH thin films, evolved by overlayers growth of carefully chosen semiconductors, with suitable band gap energies and band edge locations, offer enhanced absorption of light, significant gain in charge separation kinetics and lowered recombination losses; thus, overcoming multiple inter-woven inherent problems of single-material electrodes and finding application as efficient photoelectrode/photocatalyst [26–29].

This study is in furtherance of earlier recently published reports by authors on PEC water splitting using thin-film electrodes, CuO/Cu–ZnO and ZnO/Ag-(α)Fe₂O₃, which had produced significant gain in photocurrent generation. Herein, we are presenting the synthesis and characterization of another uniquely fabricated promising BNH thin-film photoelectrode, WO₃/Yb–Mo–BiVO₄, for application in PEC water splitting (Table 1). Mo and Yb incorporation in BiVO₄ are aimed to increase the charge separation efficiency [30, 31]. Intrinsic electron transition between O and Yb orbitals is also expected to raise absorption in the visible light region [32]. Further, the conduction band of BiVO₄ being more negative than the conduction band of WO₃, in the evolved hetero-structure efficient ejection of photogenerated electrons from BiVO₄ to WO₃ is possible. Thus, the unique part of this study and the samples synthesized are Yb and Mo co-incorporation in BiVO₄ along with the formation of hetero-junction with WO₃ that has yielded thin-film photoanodes showing significant rise in PEC water-splitting efficiency. Compared to monolayered pristine films of WO₃ and BiVO₄, the BNH films yielded 45 and 350% increment in PEC photocurrent density (I_{ph}), respectively, and could successfully surmount the limitations of charge carrier recombination in pristine materials. Incorporation of optimized doses of Yb and Mo in BiVO₄ overlayer of Yb–Mo–BNH films led to further boost (~130%) in I_{ph} , largely attributable to more efficient charge transfer kinetics across the junction.

2 Materials and methods

Analytical Grade reagents (purity 99.9%) and double-distilled deionized water (specific conductance < 10⁻⁶ Ohm⁻¹ cm⁻¹) were used. Conducting glass plates (FTO, fluorine-doped tin oxide, Sigma-Aldrich, 2.3 mm thick) of dimension 1.5 cm × 1.5 cm and sheet resistance ~ 14 Ω cm⁻² were used as substrate to grow films under pre-optimized conditions, ensuring uniform and continuous deposition.

3 Synthesis

3.1 Pristine WO₃ thin films

WO₃ thin films were prepared by drop-cast method. FTO plates were cleaned by soaking in ethanol–acetone solution (1:1 V/V) under sonication for 10 min followed by washing with water and air-drying. Precursor solution (PS) was prepared by dissolving ammonium paratungstate (APT, 0.77 M, (NH₄)₁₀H₂(W₂O₇)₆·4H₂O) and polyvinylpyrrolidone (PVP, 3 mM, (C₆H₄NO)₉) in deionized water. Thin films of PS were drop-casted over FTO substrate with the help of roller, followed by drying in oven at 120 °C for 20 min and sintering in air at 500 °C for 2 h [33].

3.2 Pristine BiVO₄ and Yb–Mo–BiVO₄ thin films

BiVO₄ thin films were synthesized by ultrasonic spray pyrolysis, using PS of bismuth nitrate pentahydrate (BNP, (Bi(NO₃)₃·5H₂O, 3 mM) and ammonium metavanadate (AMV, NH₄VO₃, 3 mM), prepared in 2 M nitric acid under continuous stirring for 1 h. PS was spiked with calculated quantities of ammonium molybdate polyhydrate (AMP, (NH₄)₂MoO₄·nH₂O) and ytterbium nitrate pentahydrate (YNP, Yb(NO₃)₃·5H₂O) to obtain Yb–Mo–BiVO₄ thin films at 2% Mo and varying levels (1, 2, 4 and 6%) of Yb incorporation. PS was sprayed onto pre-heated (~80 °C) FTO plates using ultrasonic spray coater (SonoTek Corporation, USA) under air pressure 2 psi (~13.79 kN m⁻²) and solution flow rate 0.02 cm³ min⁻¹. Post-deposition, the prepared films were air-sintered at 500 °C for 2 h.

3.3 WO₃/BiVO₄ and WO₃/Yb–Mo–BiVO₄ bilayered thin films

BNH (WO₃/BiVO₄) and Yb–Mo–BNH (WO₃/Yb–Mo–BiVO₄) thin films were synthesized by spray coating BiVO₄ overlayer (with and without Yb–Mo incorporation) onto pre-deposited WO₃ films. Process and deposition parameters of film growth were same as enumerated above.

Prepared films were stored away from moisture at low temperatures (~10 °C) in air-tight containers and characterized for crystallographic, optical, morphological and other semiconductor properties of significance for their slated role as photoelectrode in PEC cell.

3.4 Characterization

Surface profilometer (Tencor Alpha Step D-120) was used to measure film thickness (t). Bulk density was estimated from the weight/volume ratio [4]. Electrical resistivity (r) was determined *in situ*, using films as working electrode (WE), in

conjunction with saturated calomel reference electrode (SCE) and platinum counter electrode (CE), in a single compartment quartz vessel PEC cell, filled with aqueous solution (200 cm³) of K₂HPO₄ (1.0 M, pH 8.7, temperature 31 ± 3.6 °C), connected to electrochemical work station (EWS; PP211, CIMPS-pcs, Zahner, Germany). Using Eq. 1 and slope of current (*I*)–voltage (*V*) plot, measured beyond breakpoint under darkness, *r* was computed, with approximation that the measured resistance in the cell circuit is contributed only by thin-film sample, whilst CE and electrolyte contribute only negligible resistance [34]. Here, *A* and *R* represent geometrical area and resistance of film, respectively.

$$r = AR/t \quad (1)$$

Double-beam UV–Visible spectrophotometer (UV-2450, Shimadzu, Japan) was employed to investigate light absorption characteristics of thin films in wavelength range 350–800 nm, using bare FTO substrate as reference. Tauc plots were generated from absorption data using Eq. 2 to estimate band gap energy (*E_g*). Here, *α* is the light absorption coefficient, *C* is a constant, *hν* is the energy per photon and *n* is an integer with values of 1 and 4, respectively, for direct and indirect band gap energy [35, 36].

$$\alpha h\nu = C(h\nu - E_g)^{n/2} \quad (2)$$

Photoluminescence characteristics of representative samples were examined using Horiba FluoroMax-4 Spectrophotometer (Fluorolog 3–21, Jobin Yvon).

Bruker AXS D8 advance (Germany) X-ray diffractometer (XRD) equipped with Cu K α radiation ($\lambda = 1.5418 \text{ \AA}$), mirror at fixed incidence angle of 1–5°, angular resolution 0.01° and angular accuracy 0.001° was used to investigate crystal phase and micro-structural properties of films. Scanning angle (2θ) was varied in the range 20–60°, with 0.02° per min step size. Using Eq. 3, average crystallite size (*t*) was determined through Debye–Scherrer computation. Equations 4–6 were employed to estimate dislocation density (*d*), microstrain (γ) and lattice strain (ζ) in crystal structure [37]. Here, β is the full width of peak at half maximum, θ is the half diffraction Bragg angle of peak centroid and *n* is a constant with value 0.9.

$$t = n\lambda/\beta\text{Cos}\theta \quad (3)$$

$$d = 1/t^2 \quad (4)$$

$$\gamma = (\beta\text{Cos}\theta)/4 \quad (5)$$

$$\zeta = (\beta\text{Cos}\theta)/4\text{Sin}\theta \quad (6)$$

Atomic Force Microscope (AFM, Nanosurf easyscan, Version 1.8, Switzerland) was used to explore the surface

topography of films, which is critical in the PEC cell performance of films. AFM images (256 × 256 data points) were recorded by scanning 5 μm × 5 μm area of film surface at applied force 20 μN. AFM data were used to compute Root Mean Square (RMS) surface roughness (*S_a*) values for films.

Surface morphology of films was investigated by recording images at varying magnifications using field-emission scanning electron microscope (FE-SEM, JEOL JSM-7610F). For representative BNH film sample (WB4), cross-section SEM images were recorded to observe actual growth of nano-hetero-structure at WO₃/BiVO₄ junction. Further, by analysing 60–80 randomly chosen particles in SEM images, through ImageJ software, distribution of particle size in the prepared samples was tentatively drawn.

Energy-Dispersive X-Ray (EDX) analysis of films was undertaken at 5–7 randomly chosen points extended over the film surface, using OXFORD EDS LM2 unit attached to FE-SEM, to generate average elemental composition at ± 5.6% standard deviation. Exploring further the oxidation states of different elements in films, representative sample was subjected to X-ray photoelectron spectroscopy (XPS). High-resolution XPS (PHI 5000 Versa Probe III) equipped with Mg-K α radiation, AES Module with Ar ion and C60 sputter guns (PHI 5000 Versa Probe II, FEI Inc.) and overall energy resolution 0.7 eV was used in the analysis.

Corroborating crystallographic and compositional characteristics of thin films, the sample yielding highest PEC response was subjected to TEM analysis using JEOL JEM-1400 Transmission Electron Microscope (TEM). The instrument was fitted with large area SDD detectors with compact foot print, LaB6 single-crystal tip, 120 kV maximum accelerating voltage, ± 70° tilted computer controlled stage and TEMCON software.

3.5 PEC studies

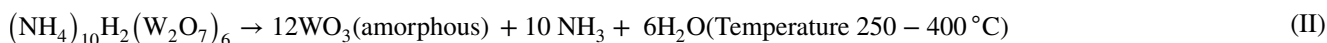
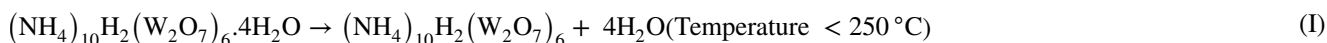
Ohmic electrical contact was established in the prepared thin films using the method described elsewhere [38] and these were used as working electrode (WE), in conjunction with saturated calomel reference electrode (SCE) and platinum counter electrode (CE), in PEC studies. Single compartment quartz vessel PEC cell was filled with aqueous solution (200 cm³) of K₂HPO₄ (1.0 M, pH 8.7, temperature 31 ± 3.6 °C). Xenon Arc Lamp (150 W, Oriel, USA) was employed to illuminate the surface of WE at illumination intensity of 130 mW cm⁻² (equivalent to 1.5 Sun intensity). To eliminate any possible interference, dissolved air in the electrolyte solution was flushed out by purging it with nitrogen gas for 20 min, just prior to each PEC measurement. For the PEC cell fabricated, linear sweep voltammetry (LSV) plots of current (*I*) vs. potential (*V*) were recorded, under darkness and illumination, using EWS (PP211, CIMPS-pcs, Zahner, Germany) and applied *V* (vs. SCE) varied from -1.0 to +1.0 V at scan

rate of 20 mV/s [39]. The area of WE exposed to electrolyte was 1 cm². From *I*–*V* plots, open-circuit voltage (*V*_{oc}) and short-circuit current (*I*_{sc}) were estimated. Rise in current under illumination, against darkness, led to the photocurrent density values (*I*_{ph} = *I*_{illumination} – *I*_{darkness}). Applied bias photon-to-current efficiency (*ABPE*) of the PEC cell was computed using Eq. 7.

$$ABPE = [I_{ph} \times (1.80 - V_b) / P] \times 100 \quad (7)$$

Here, *P* is the illumination power intensity (mW cm⁻²) and *I*_{ph} is in mA cm⁻². The applied bias (*V*_b) is the difference between *V*_{meas} and *V*_{oc}, where *V*_{meas} is the potential (vs. SCE) of WE at which the *I*_{ph} is recorded [40]. Although, the minimum required potential for water splitting is 1.23 V, but due to overpotential and other losses in the circuit, the value shoots to 1.80 V and the same has been used in Eq. 7 to compute *ABPE*.

Electrochemical impedance measurement was undertaken for PEC cell, using LCR meter (Agilent Technolo-



gies, Model 4263B), under darkness at lowest possible AC voltage amplitude (~5 mV, comparable with *V*_{oc}) in the frequency range 100 mHz to 10 kHz. From Eqs. 8–9 and observed variations in space charge capacitance (*C*_{sc}) with *V*, Mott–Schottky (MS) plots were generated, which led to flat band potential (*V*_{fb}) and charge carrier density (*N*_d) for thin-film electrodes. Here, *q* is the electronic charge, *T* is the absolute temperature, *k*_B is the Boltzmann's constant, *S* is the slope of MS plot, *A* is the electrode surface area (1 cm²), *ε*_s is the permittivity of the semiconductor which is in contact with electrolyte, and *ε*₀ is the permittivity of free space (8.85 × 10⁻¹² F/m for vacuum) [41].

$$1/C_{sc}^2 = [2/(\epsilon_0 \epsilon_s A^2 q N_d)] [V - V_{fb} - (k_B T / q)] \quad (8)$$

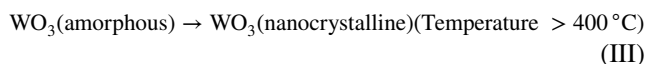
$$S = 2/(\epsilon_0 \epsilon_s q N_d) \quad (9)$$

Exploring charge transfer kinetics at semiconductor electrolyte interface, Nyquist plots were obtained using EWS (PP211, CIMPS-pcs, Zahner, Germany) at AC voltage amplitude 5 mV, AC frequency 1 kHz in sweep mode and 100 mHz to 10 kHz applied frequency.

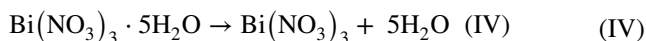
4 Results and discussion

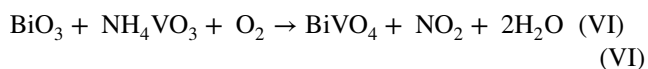
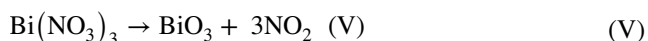
4.1 Film synthesis

Evolution of WO₃ from APT, the precursor compound used in the synthesis of monolayered pristine films of WO₃ (sample WP) and underlayer of WO₃ in BNH and Yb-Mo-BNH films is temperature dependent. The reaction occurs in three temperature zones. At <250 °C, mainly water molecules are released. In the temperature range 250–400 °C, water molecules and ammonia are released along with evolution of amorphous WO₃ through restructuring of W and O atoms. At > 400 °C crystallization proceeds, where again depending upon the temperature, nanocrystallites of WO₃ of varying dimensions evolve. PVP, which is a water soluble polymer with good adhesive and binding properties, works as stabilizer for PS and its optimal concentration in the solution facilitates thin-film formation on FTO substrate. Tentative set of reactions, (I)–(III), for the evolution of WO₃ film are written below.



In the synthesis of monolayered pristine films of BiVO₄ (sample BP) and overlayer of BiVO₄ in BNH and Yb-Mo-BNH films, BNP and AMV were used as precursors. Both the compounds are easily soluble in 2 M nitric acid and yielded stable solution. Besides the concentration of precursor compounds in solution, temperature is a critical variant for the growth of nanocrystallites and to regulate size of particles. Thus, post-deposition sintering is a vital step in the evolution of BiVO₄ films. Sintering at elevated temperatures generally promotes the growth of finer particles. However, at very high temperatures, coalescing of particles is also reported [41, 42]. Tentative set of reactions, (IV)–(VI), for the evolution of BiVO₄ films are proposed hereunder. YNP and AMP used to incorporate Yb and Mo, respectively, in BiVO₄ layer are readily soluble in the solvent used and the generated by-products are easily removable through post-deposition sintering.





4.2 General characteristics

Prepared thin films were stable and did not peel off when put in contact with electrolyte solution in PEC cell. The average thickness of bilayered films is 640–730 nm against 410 and 260 nm, respectively, for monolayered pristine WO_3 and BiVO_4 films. Observed bulk density of synthesized films compared against true density of pure WO_3 ($4.1\text{--}4.4 \text{ g cm}^{-3}$) and BiVO_4 ($6.0\text{--}6.4 \text{ g cm}^{-3}$) reveals mesoporous character of samples, with 52–66% porosity (Table 1) [41]. Temperature played major role in evolution of nanocrystallites and particle size regulation, thereby affecting density and thickness of films (Table 1) [42]. Film thickness and density were observed to vary inversely, as compact and dense growth of nanocrystallites yielded thinner films. Further downslide in density on Yb and Mo incorporation is suggestive of their likely diffusion in BiVO_4 overlayer, causing partial disruption/opening-up of the host lattice due to significant difference in ionic radii of Bi^{3+} (110 pm), Yb^{3+} (101 pm) and Mo^{6+} (73 pm) ions [43]. Film porosity is critical in their use as photoelectrode in PEC cell, especially to form effective contact with electrolyte solution. The n-type nature of both pristine WO_3 and BiVO_4 thin films, as indicated from $I\text{--}V$ plots, indicates oxygen vacancies and/or metal interstitials in the lattice, possibly due to crystal growth being partially non-stoichiometric. Compared to monolayered pristine thin films of BiVO_4 , pristine WO_3 films recorded higher *in situ* electrical resistivity (r), which is on expected lines [44]. Incorporation of Mo and Yb in BiVO_4 films possibly created more acceptor sites, thereby yielding significant fall in r . Further, compared to monolayered pristine thin films of WO_3 and BiVO_4 , bilayered films recorded noticeable drop in r , with further fall in the value on Yb and Mo incorporation in BiVO_4 overlayer (Table 2). Besides, the expected rise

in acceptor sites, the effect is also attributable to increase in native defects, which was seemingly highest in sample WB4 [45]. It is also evident that decrease in r has seemingly played direct role in raising the PEC performance of films.

4.3 Optical characteristics

Figure 1 displays light absorption characteristics of prepared thin-film samples in the frequency range 350–800 nm. Whilst monolayered pristine films of BiVO_4 (sample BP) depicts significant absorption in the entire visible–ultraviolet region, monolayered pristine WO_3 films (sample WP) absorbs in near UV and UV regions. Absorption thresholds for sample WP and BP fall at ~ 480 and ~ 720 nm, respectively, in accordance with their reported band gap energies [46]. The photoluminescence data for these samples (Fig. 1) are also in tune with the above observations. In WO_3 the absorption edge corresponds to O 2p \rightarrow W 6s excitation with an indirect band gap, which is typical for several other metal oxides as well. However, in BiVO_4 the interaction between O 2p and Bi 6s is known to create upward dispersion of valence band away from Brillouin zone centre with relatively light hole effective mass. Further, the coupling of O 2p and Bi 6p levels with unoccupied V 3d states leads to conduction band minimum at the zone edge, maintaining low energy direct transitions [47]. Marginal red shift in the absorption edge of BiVO_4 is noticeable on Yb–Mo incorporation. Absorption magnitude, which is largely exciton regulated, is significantly higher in bilayered films against monolayered pristine films and is indicative of contributions from both, the WO_3 underlayer and BiVO_4 overlayer. Incorporation of Yb and Mo in BiVO_4 overlayer of BNH films led to further rise in absorption magnitude. Band gap energies estimated from Tauc plots (Fig. 1, Table 2) are in agreement with the earlier reported values [48]. Slight fall in the band gap energy on Yb and Mo incorporation could be due to increase in oxygen vacancies and electron concentrations, arising from difference in electronegativity (Bi: 2.02, Yb: 1.10, Mo: 2.16) and ionic radii of cations [49].

Table 2 Electrical resistivity (r), average crystallite size (s), microstrain (γ), lattice strain (ζ), dislocation density (η), band gap energy (E_g) and RMS surface roughness (S_a) values for films

Sample	$r \times 10^3$ ($\text{k}\Omega \text{ cm}$)	s (nm)	$\gamma \times 10^4$	$\zeta \times 10^4$	$\eta \times 10^{-15}$ ($\text{line}^2 \text{ m}^{-2}$)	E_g (eV)	S_a (nm)
WP	3.11	37	0.70	3.33	0.70	2.85	11
BP	2.45	32	0.64	2.60	0.90	2.38	12
B1	1.85	29	0.72	2.91	1.22	2.31	21
B2	1.56	25	0.81	3.27	1.54	2.35	27
B4	1.12	31	0.65	2.63	1.00	2.28	43
B6	1.63	42	0.48	1.96	0.56	2.32	28
WB	1.35	27	0.77	3.70	1.40	2.22	35
WB4	0.64	22	0.92	4.40	1.98	2.10	51

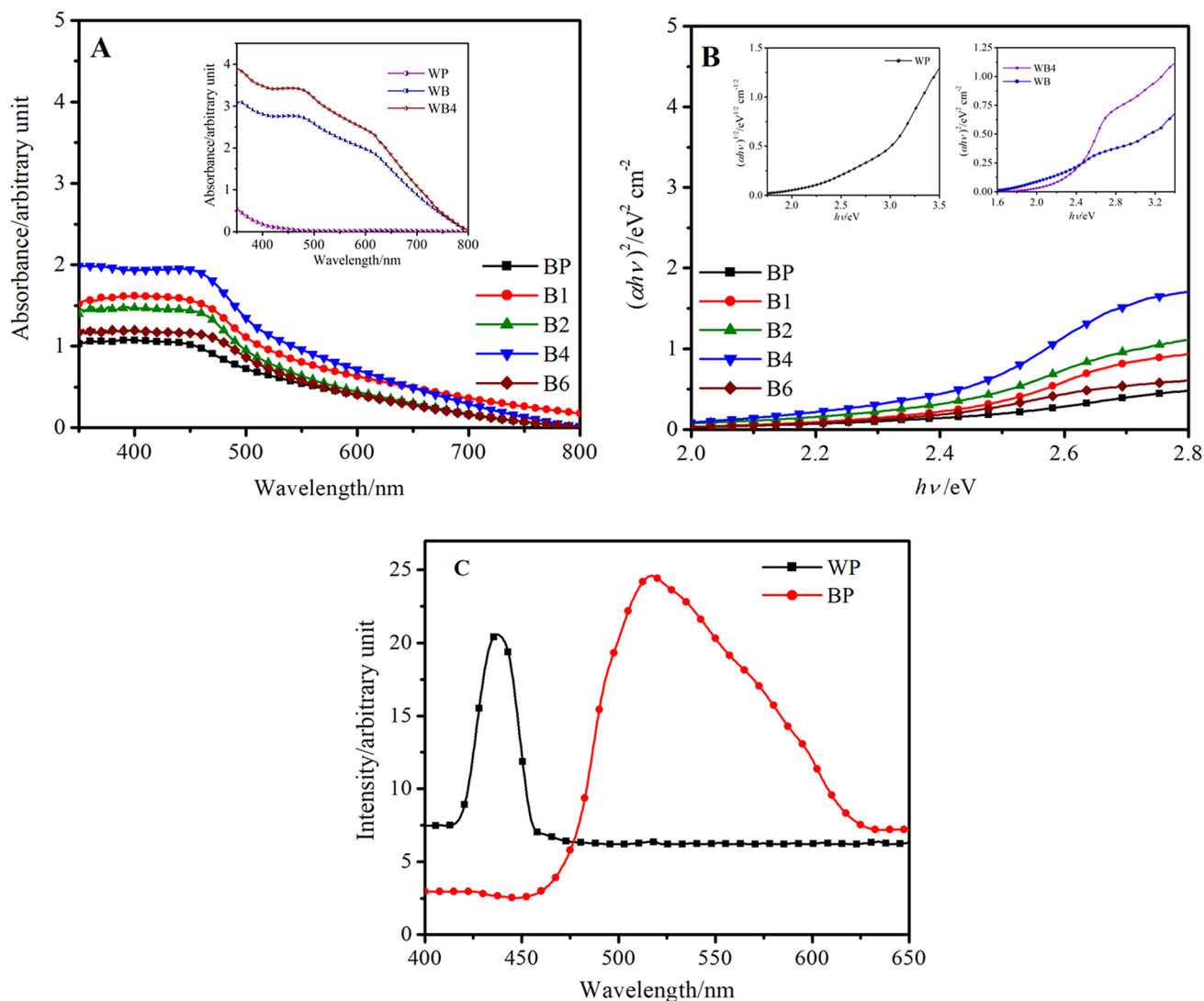


Fig. 1 Absorption vs. wavelength plots (**A**) and Tauc plots (**B**) for pristine and bilayered thin films; photoluminescence plots (**C**) for pristine samples

4.4 Crystallographic characteristics and microstructure

Multiple peaks seen in the observed XRD pattern indicate polycrystalline nature of films (Fig. 2). Peaks recorded at 2θ angles 28.8, 30.7, 34.9, 39.8 and 47.1° correspond to diffractions from (121), (040), (200), (211) and (042) planes of monoclinic BiVO₄ (space group I2/a; lattice constants: $a = 5.10 \text{ \AA}$, $b = 5.13 \text{ \AA}$, $c = 11.63 \text{ \AA}$; JCPDS card 14–0688). Likewise, peaks at 2θ angles 23.5, 24.3, 34.1, 41.5, 54.6 and 55.6° are indexed to (002), (200), (022), (222), (204) and (240) planes, respectively, of monoclinic WO₃ (space group P2₁/c; lattice constants: $a = 7.32 \text{ \AA}$, $b = 7.54 \text{ \AA}$, $c = 7.67 \text{ \AA}$; JCPDS card 83–0950). All other peaks in the pattern are ascribable to underlying FTO substrate. There is no indication on the evolution of YB-Mo-BiVO₄ solid

solution or any mixed oxides, as seen in earlier studies on hetero-junction films [50]. Unlike previous studies where Yb doping in BiVO₄ resulted in structural transition from monoclinic (space group I2/a) to tetragonal structure (space group I41/amd), crystal structure remained unaffected here [51]. Exploring the microstructure further, XRD data were used to evaluate average crystallite size (s), microstrain (γ), lattice strain (ζ) and dislocation density (η) values (Table 2). Increased strain in bilayered films (sample WB) compared to monolayered pristine films (samples WP and BP) suggests part intrusion of WO₃ and BiVO₄ lattices at hetero-junction. Significant difference in ionic radii of host lattice cation, Bi³⁺ (110 pm), and the incorporating cations, Yb³⁺ (101 pm) and Mo⁶⁺ (73 pm), is apparently accountable for building strain and dislocation density in film samples B1–B6 and WB4. Strain in the lattice, which is also evident

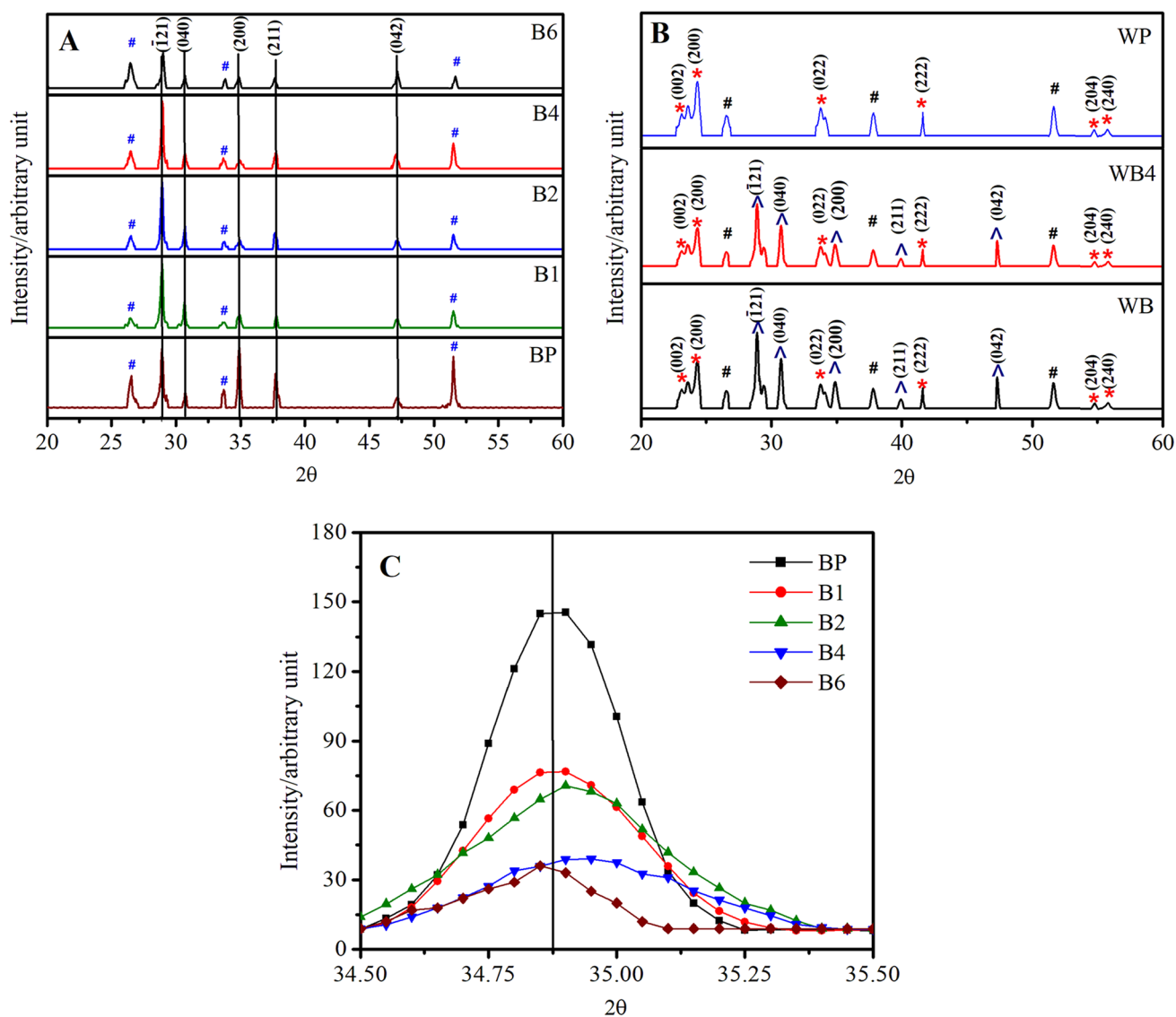


Fig. 2 XRD pattern of prepared thin films (**A**, **B**) and observed shift in (200) plane peak of BiVO_4 in bilayered films. Peaks correspond to WO_3 (*), BiVO_4 (^), and FTO substrate (#)

from significant shift in (200) peak of BiVO_4 at 2θ 34.9° (Fig. 2), is often detrimental to the growth of nanocrystallites. Revalidating the statement, average crystallite size in thin-film samples estimated through Debye–Scherrer computations, depicts inverse correlation with strain and dislocation density in the lattice.

4.5 Surface characteristics

Film surface topography is a critical variant that influences PEC cell response of thin-film electrodes. It influences the effective surface area of electrode in contact with electrolyte to regulate absorption of light and kinetics of charge transport across electrode–electrolyte junction. AFM images of

prepared thin films (Fig. 3) indicate continuous and smooth growth of nanocrystallites. RMS surface roughness (S_a) estimated from AFM data (Table 2) indicates that roughness increases significantly on incorporation of Yb and Mo, with highest value (51 nm) recorded for sample WB4. Increase in surface roughness would raise effective surface area of film electrodes exposed to electrolyte solution in PEC cell, in tune with earlier observations [52]. Top view FE-SEM images of prepared thin films and cross-section image of representative sample WB4 (Figs. 4–5) indicate the evolution of nano-structured morphology with bilayered configuration. Besides the dense growth of smaller particles underneath, the top layer is represented by the evolution of irregular rod-shaped particles in sample WP and irregular plate-like

Fig. 3 AFM images of pristine and bilayered thin films

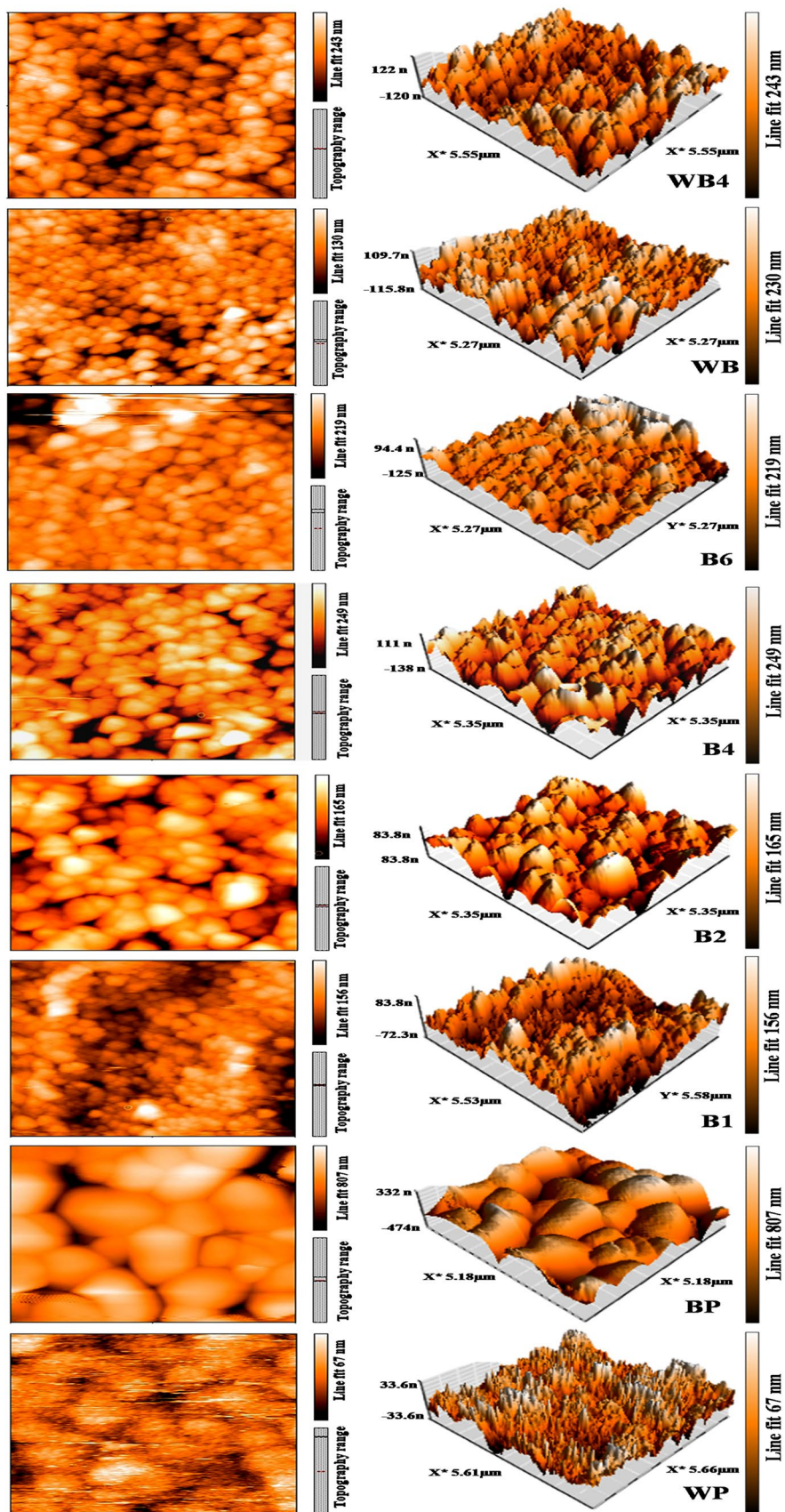
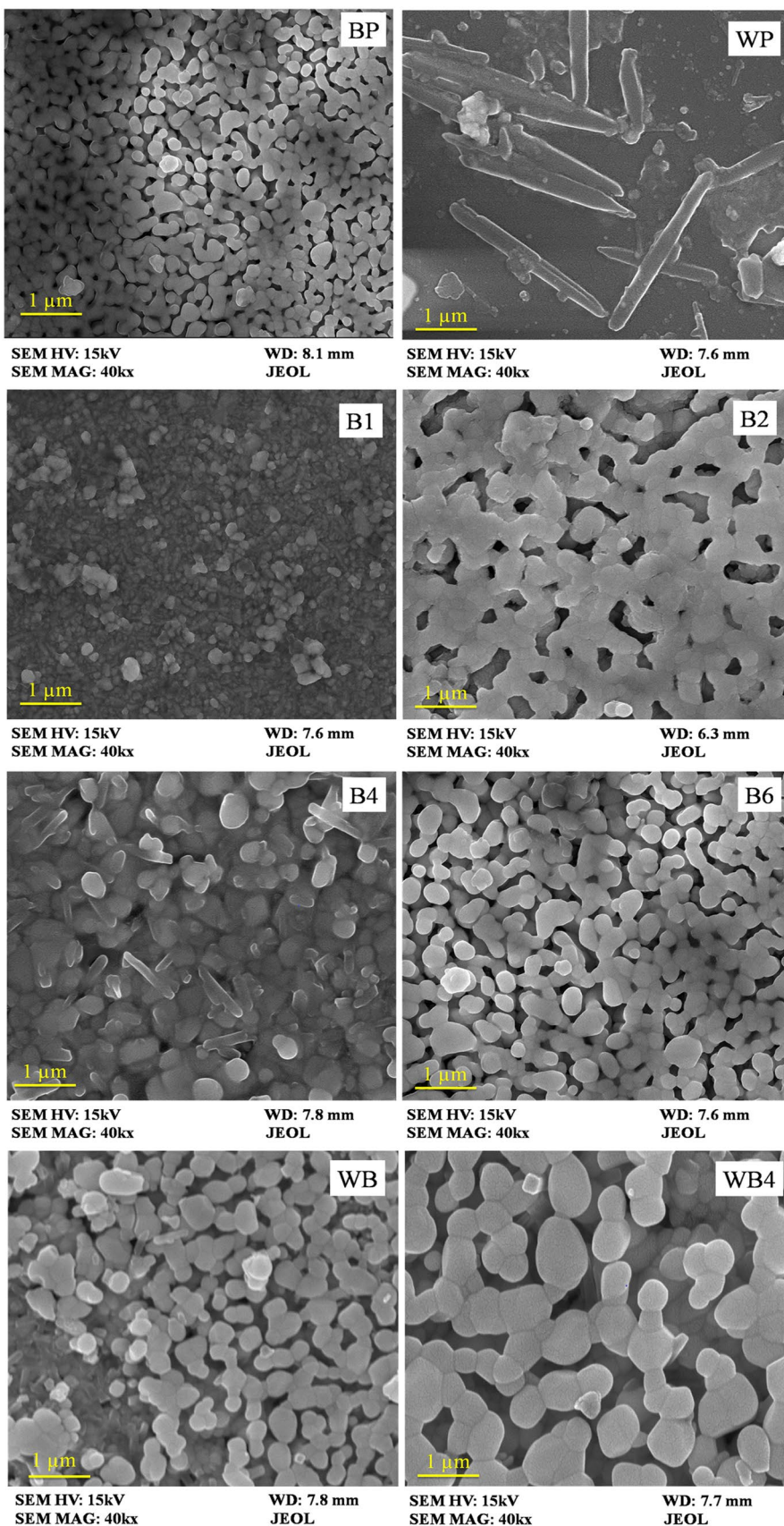


Fig. 4 FE-SEM images of pristine and bilayered thin films



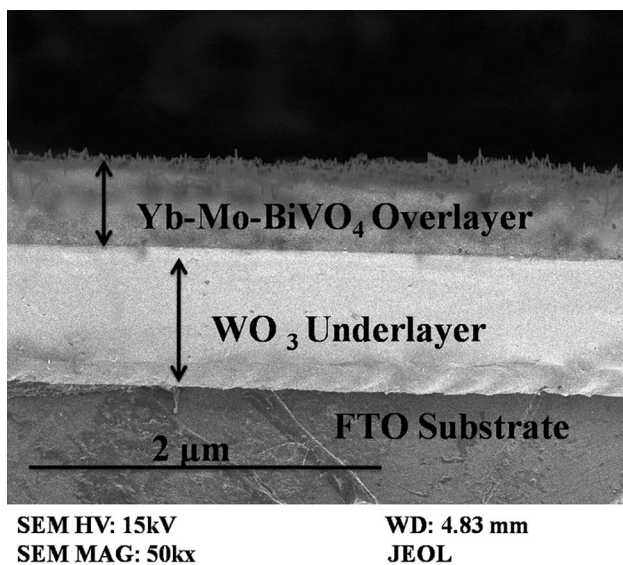


Fig. 5 Cross-sectional SEM image of sample WB4

structures in all other samples with BiVO₄ overlayer. Distribution of particle size, derived from SEM images through ImageJ software, is presented in Fig. 6. Slight disagreement in the particle size obtained from SEM images and the average crystallite size derived through Debye–Scherrer computations using XRD data suggests some grain agglomeration in samples.

4.6 Elemental composition

EDX analysis reveals elemental composition of films (Figs. 7–8) and indicates the existence of W, Bi, V, Mo, Yb and O elements. The data were used to assess prevailing atomic ratio of W, Bi, V and O that was found attuned to the formation of WO₃ and BiVO₄ phases (Table 3). Minor presence of Mo and Yb is also in accordance with induced changes in their concentration during film growth. Investigating further the surface chemical environment and oxidation states of different elements, XPS analysis of representative thin-film sample (WB4) confirmed the presence of O, Bi, V, W, Mo and Yb (Fig. 9). To standardize the binding energy of observed peaks, C 1 s (286 eV) peak was taken as reference. Bi 4f core spectrum observed with peaks at 159.3 and 164.4 eV corresponds to 4f_{7/2} and 4f_{5/2}, respectively. Similarly, V core spectrum presents peak at 516.2 eV, corresponding to V 2p_{3/2}. Observations validate chemical composition and oxidation state of Bi³⁺ and V⁵⁺ in BiVO₄. W 4f core spectrum peaks at 34.8 and 37.8 eV correspond to 4f_{7/2} and 4f_{5/2}, respectively, confirming W⁶⁺ in tune with

formation of WO₃. Although not indicated in XRD analysis, presence of Mo⁶⁺ and Yb³⁺ is confirmed through XPS analysis. Peak at 185.4 eV is indexed to Yb 4d_{5/2}, whilst Mo 3d core spectrum peaks at 233.2 and 236.2 eV correspond to 3d_{5/2} and 3d_{3/2}, respectively. Corresponding to O 1 s, two peaks are recorded. Whilst peak at 533 eV correspond to bridging oxygen in the lattices of evolved BiVO₄ and WO₃ phases; peak recorded at 535.2 eV is suggestive of hydroxyl group or chemisorbed/organic oxygen on the surface of the sample [53].

4.7 TEM analysis

Dominant evolution of monoclinic phases of WO₃ and BiVO₄ is reconfirmed from TEM analysis and the observed small area electron diffraction (SAED) pattern of representative sample (WB4) (Fig. 10). As discussed earlier, there are distinct evidences to suggest diffusion of Mo and Yb in BiVO₄ lattice, particularly during high-temperature sintering of thin films, despite significant difference in ionic radii of cations. Still, TEM analysis indicates the part presence of Yb as Yb₂O₃ and Mo as MoO₃ also possibly as nanoparticles dispersed in BiVO₄ overlayer.

4.8 PEC studies

Figure 11 presents *I*–*V* plots recorded using prepared thin films as electrode in PEC water splitting. Observed values of open-circuit voltage (*V*_{oc}) and short-circuit current (*I*_{sc}), under illumination are shown in Table 4. Figure 12 depicts variations in *I*_{ph} with applied voltage (vs. SCE). Significant increment observed in *I*_{ph} on Yb–Mo incorporation (up to 4% at. Yb concentration) in monolayered BiVO₄ films is accountable to enhanced absorption of light, charge carrier density, film surface roughness and reduced electrical resistivity. However, further increase in Yb concentration to 6% at. led to fall in *I*_{ph}, which is attributable to the space charge region becoming narrow and the penetration depth of light into the photoelectrode exceeding the space charge layer that possibly eased electron–hole recombination [50, 54]. With bilayered samples nearly 45–350% increment in *I*_{ph}, against monolayered pristine films, is largely attributable to enhanced absorption of light along with uniquely evolved microstructure and surface characteristics that favoured swift separation and migration of photogenerated charge carriers. Further, incorporating BiVO₄ overlayer with 2% Mo and 4% Yb (sample WB4), which appears to be the optimal dose, ~227–950% increase in PEC cell response is achieved, with *I*_{ph} rising to 1.67 mA cm^{−2} at 0.85 V vs. SCE. Variations in ABPE followed the same trend, with gain in value

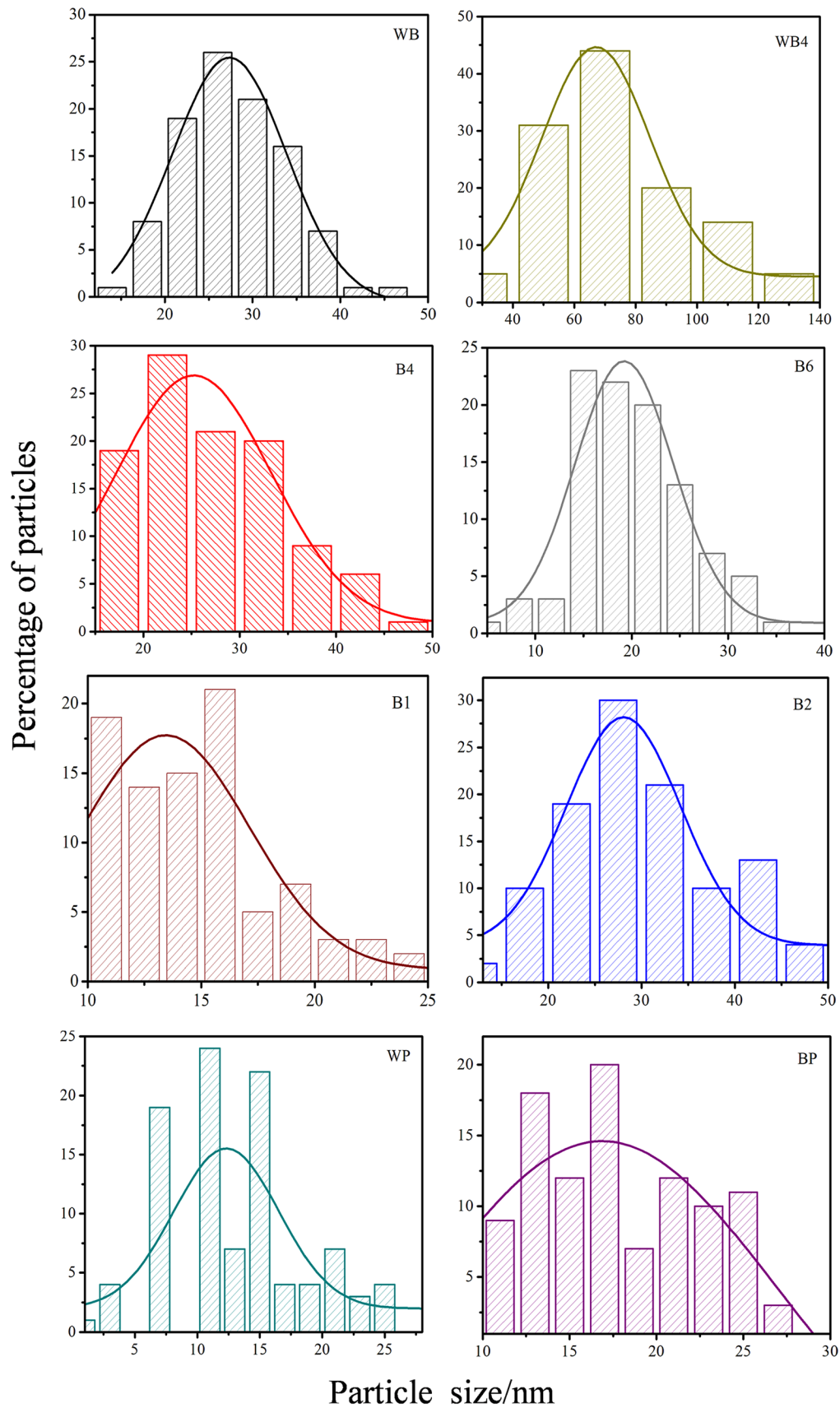


Fig. 6 Particle size distribution in pristine and bilayered thin films, as estimated from SEM data

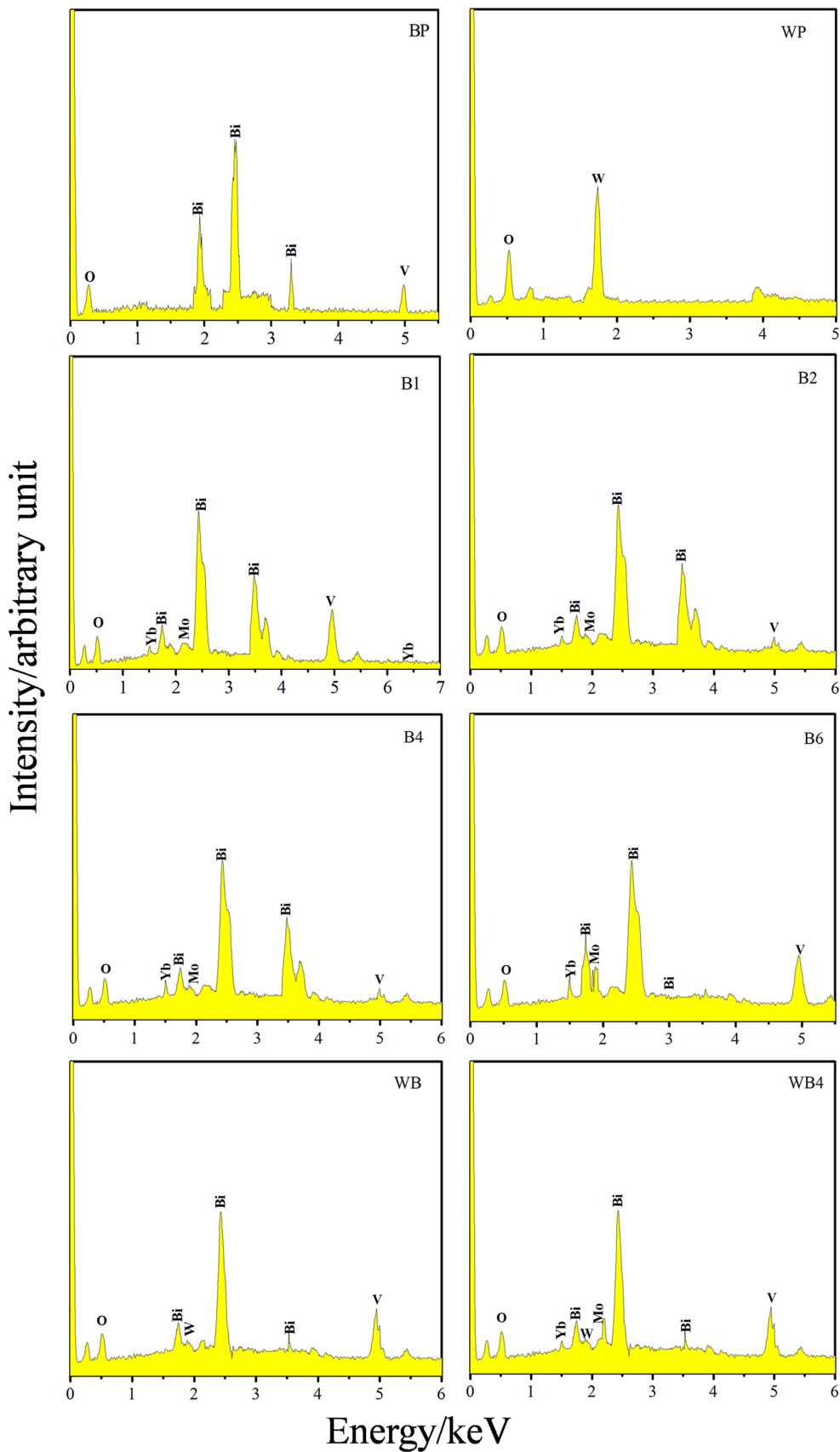


Fig. 7 EDX pattern of pristine and bilayered thin films

Fig. 8 EDX elemental mapping for thin-film sample WB4

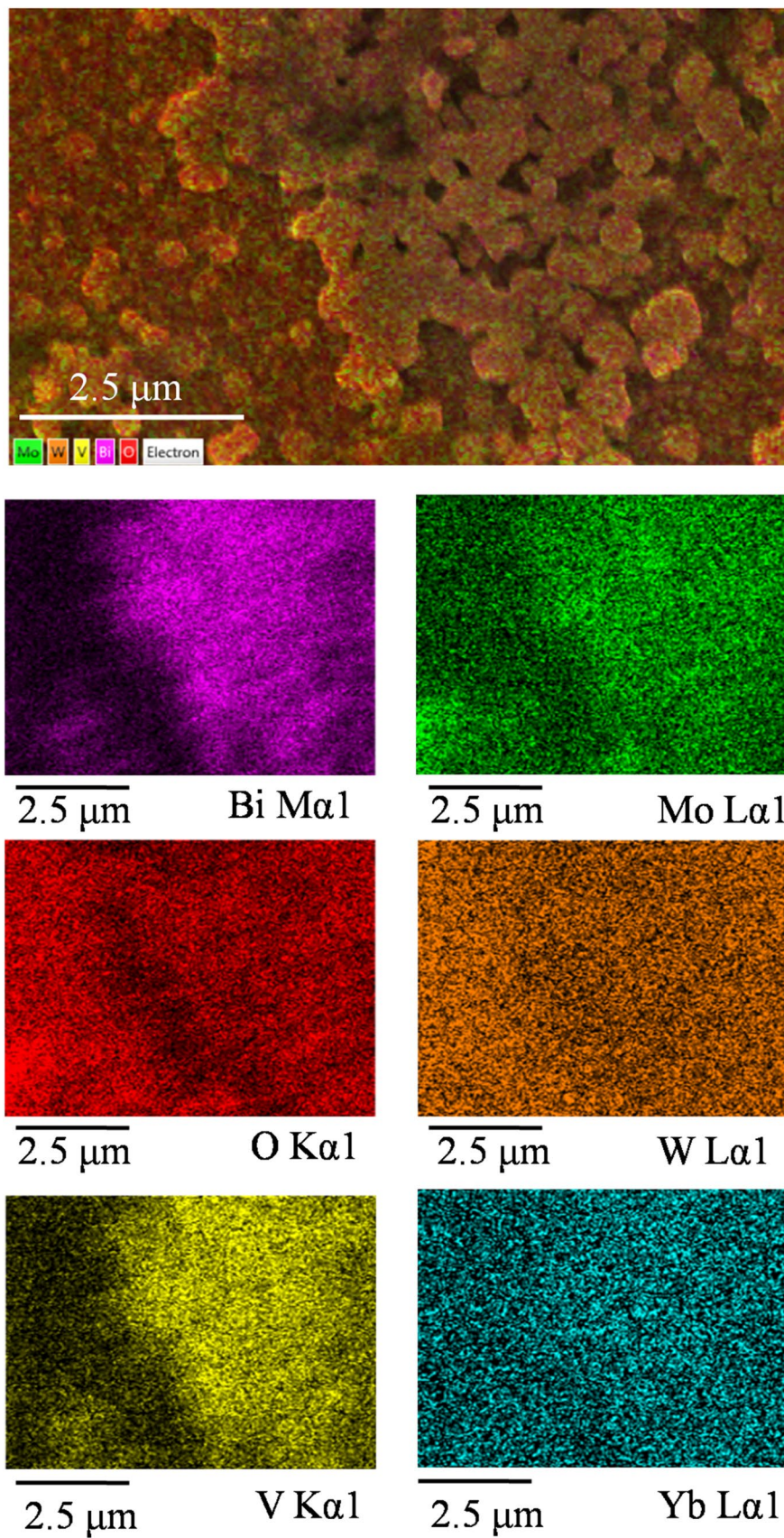


Table 3 Elemental composition of thin films observed through EDX analysis

Sample	Weight percentage*					
	O K	VK	Mo K	Yb L	Bi M	W L
WP	32.3 (78.5)	–	–	–	–	64.9 (18.8)
BP	27.6 (67.9)	12.3 (14.3)	–	–	56.9 (14.8)	–
B1	26.6 (64.6)	11.1 (13.6)	1.4 (0.6)	0.7 (0.4)	58.5 (18.2)	–
B2	25.9 (65.6)	12.7 (16.6)	1.6 (0.5)	1.4 (0.7)	55.2 (13.9)	–
B4	24.8 (64.5)	12.9 (17.3)	1.4 (0.7)	3.2 (0.9)	55.0 (13.3)	–
B6	23.7 (63.8)	13.2 (18.6)	1.5 (0.8)	5.3 (1.3)	53.9 (12.9)	–
WB	24.7 (74.7)	6.5 (8.5)	1.7 (0.6)	–	34.1 (8.4)	30.5 (6.2)
WB4	25.9 (75.2)	5.7 (8.2)	1.4 (0.5)	3.3 (0.9)	32.9 (7.9)	28.2 (5.8)

*Given in parenthesis are atomic percentage values

attributable primarily to diminished electrical resistivity, increased RMS surface roughness, high photocurrent density and high open-circuit voltage.

Variations in I_{ph} under chopped light illumination, recorded with the best performing sample WB4 (Fig. 13), confirm the role of light in PEC current generation. Usefulness of studied BNH and Yb–Mo–BNH films as photoanode in PEC water splitting is also evident from their high chemical and electrochemical stability in contact with electrolyte solution. Continuous illumination and exposure of films in PEC cell for ~60 min did not cause any harm to the electrode surface, as evident from nearly sustained results on I_{ph} and V (Fig. 13). The XRD pattern and SEM images recorded before and after PEC studies for representative sample WB4, showing insignificant changes, also indicate the stability of films (Fig. 14). Moreover, in repeat observations recorded during 12–14-month duration, I_{ph} values were observed reproducible within $\pm 5.2\%$ deviation.

Table 4 presents flat band potential (V_{fb}) and charge carrier density (N_d) values, derived from Mott–Schottky (MS) plots (Fig. 15). MS curve with positive slope are in agreement with n-type nature of thin films. A more negative V_{fb} amounts to higher band bending at the interface in heterojunction, which would reduce charge carrier recombination and boost PEC cell photoresponse [54]. Validating the contention, sample WB4 with most negative V_{fb} also recorded highest I_{ph} .

Exploring charge transfer kinetics at the electrode/electrolyte interface, Nyquist plots between real and imaginary components of impedance were drawn (Fig. 16). Semicircle of lowest radius carved out by sample WB4 confirms the charge transfer resistance across electrode/electrolyte

interface being lowest in this case, which is majorly responsible in raising the PEC cell performance of the electrode.

4.8.1 Charge transfer mechanism

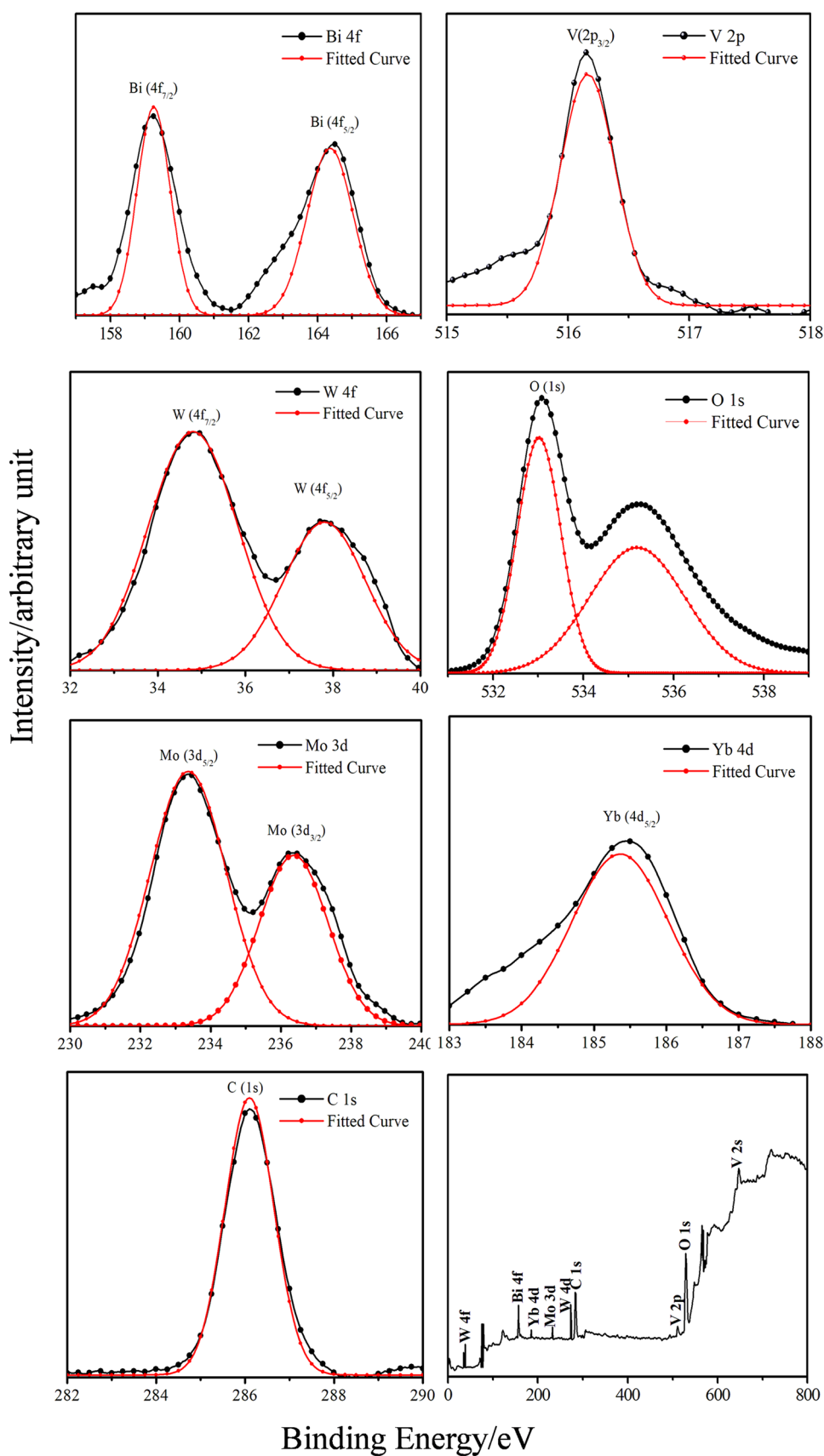
Figure 17 depicts tentative alignment of band edges in BNH thin films, along with water-splitting redox energy levels for hydrogen and oxygen evolution, before and after illumination. Conduction band (CB) and valence band (VB) edge energy locations in WO_3 and $BiVO_4$ were obtained from Butler and Ginley computations, using Eqs. 10–11. E_{cb} and E_{vb} are, respectively, conduction and valence band edge energies and E° is the energy of free electron in the hydrogen scale (~4.5 eV) [33, 54]. X is geometrical mean of absolute electronegativity of all elements in the considered oxide semiconductor.

$$E_{cb} = X - E^\circ - 0.5E_g \quad (10)$$

$$E_{vb} = E_{cb} + E_g \quad (11)$$

With n-type nature of both WO_3 and $BiVO_4$, the unique formation of n/n hetero-structure in the present case facilitated enhanced absorption of light and swift flow of photoinduced charge carriers and their participation in water splitting. Before the formation of junction, CB and VB of WO_3 lie below the respective levels of $BiVO_4$. Moreover, charge carrier concentration in WO_3 is higher in comparison to $BiVO_4$ (Table 4), which suggests that the energy separation between the Fermi level and CB in WO_3 is narrower. With this arrangement in place, in bilayered films electrons

Fig. 9 XPS spectra of pristine and bilayered thin films



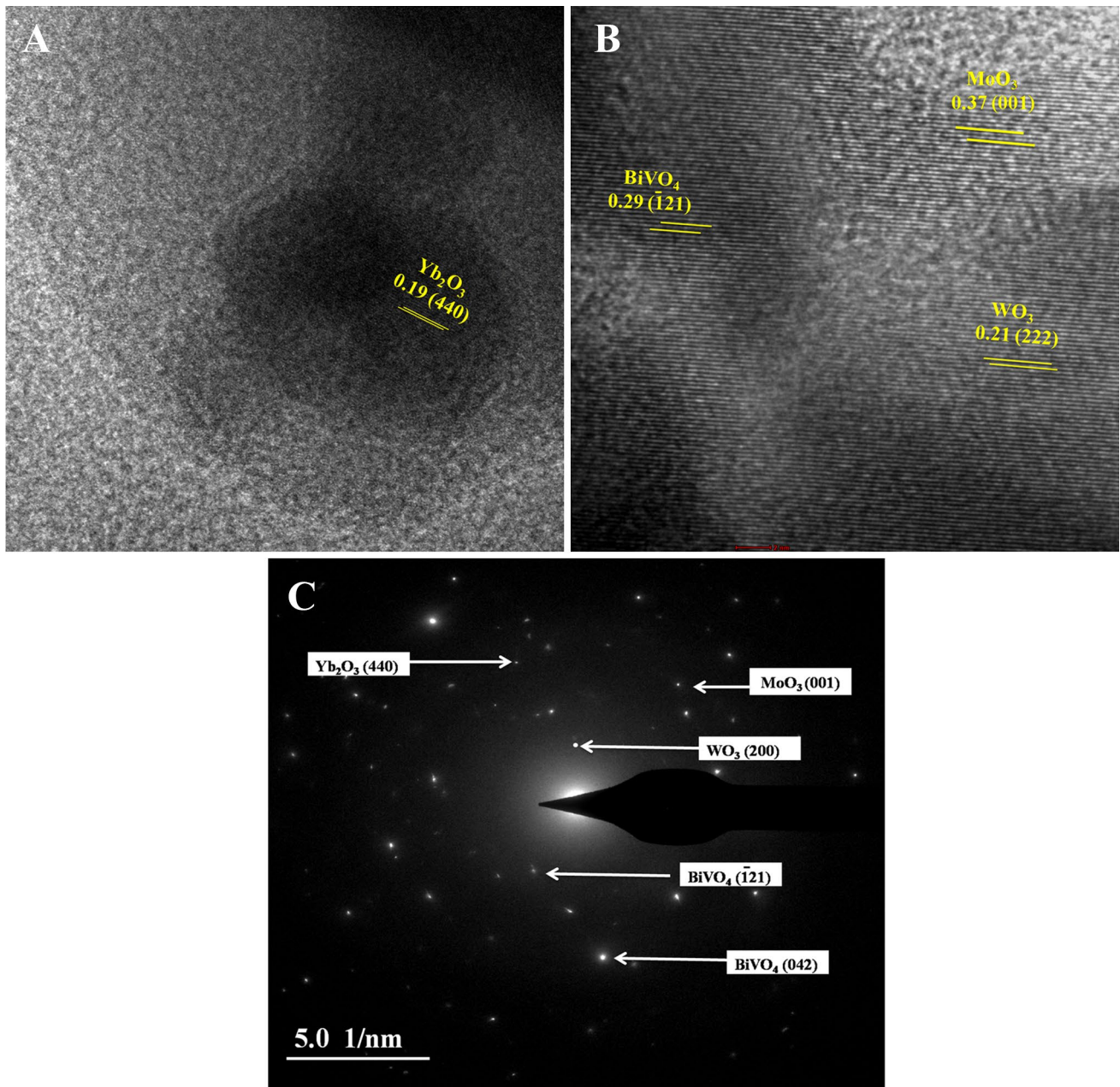


Fig. 10 TEM images (A, B) and SAED pattern (C) for thin-film sample WB4

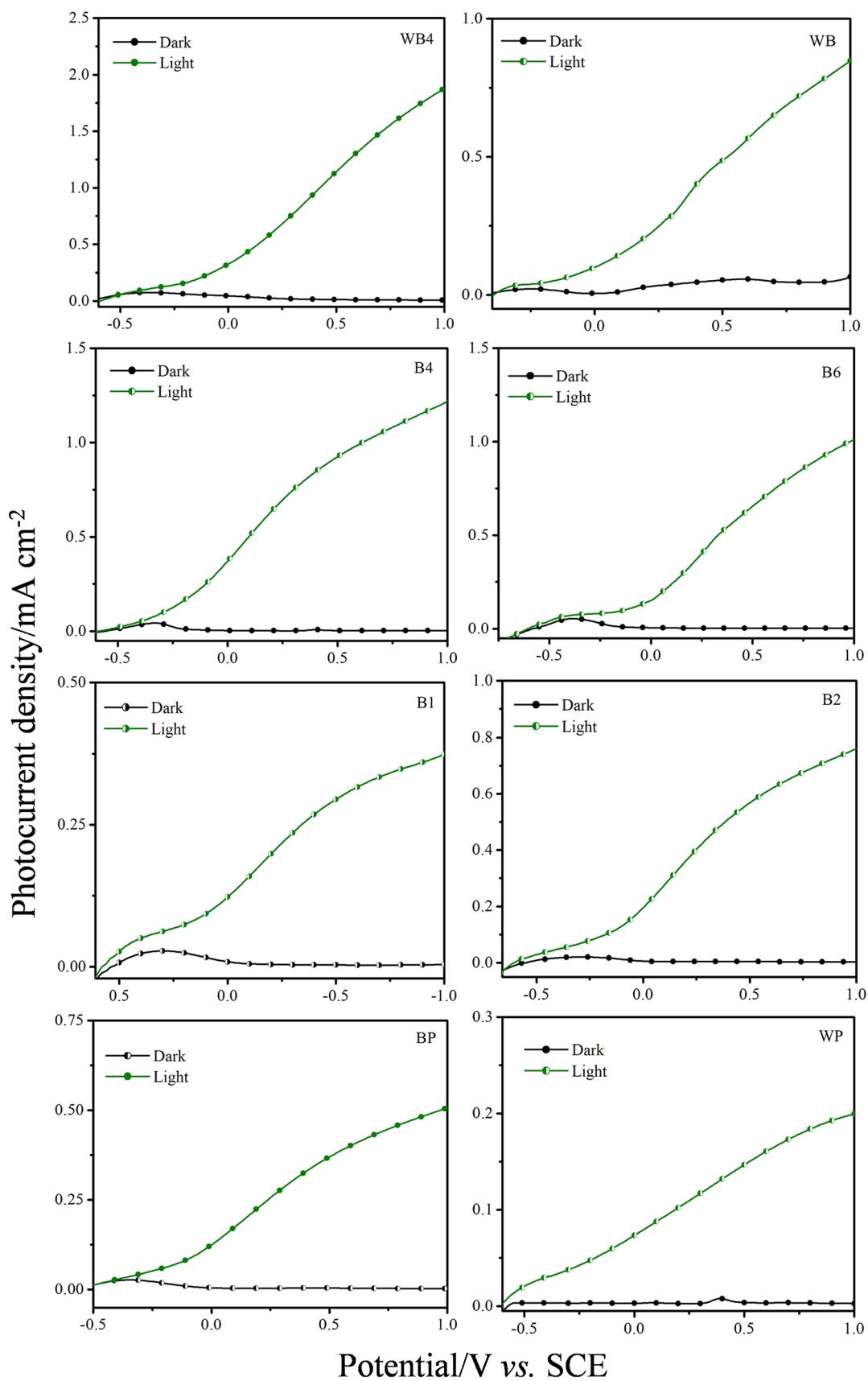


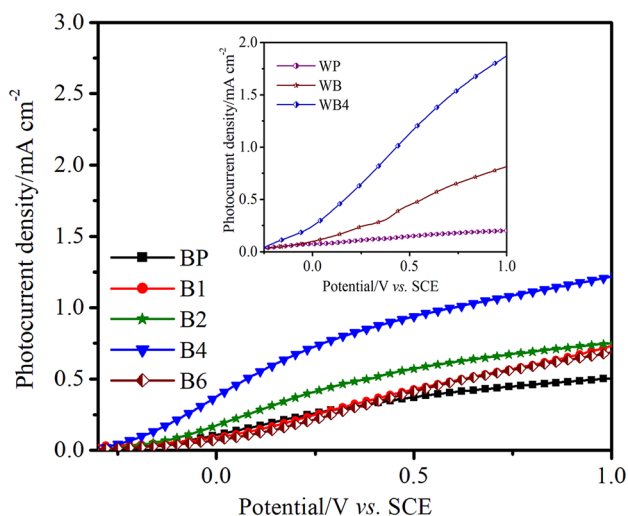
Fig. 11 $I-V$ plots for pristine and bilayered films, recorded under darkness and illumination

Table 4 Observed photocurrent density (I_{ph}), flat band potential (V_{fb}), charge carrier density (N_d) and applied bias photon to current conversion efficiency (ABPE)

Sample	I_{ph}^* (mA cm ⁻²)	V_{fb} (V vs. SCE)	$N_d \times 10^{-17}$ (cm ⁻³)	$V_{oc}^{\#}$ (V vs. SCE)	$I_{sc}^{\#}$ (mA cm ⁻²)	ABPE* (%)
WP	0.16	-0.59	2.1	-0.31	0.09	0.08
BP	0.51	-0.24	1.6	-0.27	0.11	0.27
B1	0.38	-0.26	5.6	-0.28	0.30	0.20
B2	0.71	-0.28	6.3	-0.24	0.10	0.39
B4	1.12	-0.36	7.2	-0.27	0.35	0.59
B6	0.62	-0.30	5.8	-0.22	0.16	0.35
WB	0.73	-0.50	2.6	-0.25	0.13	0.39
WB4	1.67	-0.47	3.9	-0.32	0.18	0.81

*At 0.85 V applied potential (vs. SCE)

#Under illumination

**Fig. 12** Variation in I_{ph} with applied voltage (vs. SCE) for pristine and bilayered thin films

would flow spontaneously from the Fermi level of BiVO_4 to the Fermi level of WO_3 till the Fermi levels equalize. At equilibrium, however, the CB of WO_3 would still be lower in energy compared to CB of BiVO_4 owing to smaller energy separation between the CB and Fermi level in WO_3 . Upon illumination, the photogenerated electrons in BiVO_4 would, thus, easily flow to the CB of WO_3 . Further, the step-like alignment of VB of WO_3 and BiVO_4 is favourable for spontaneous flow of photogenerated holes from VB of WO_3 and BiVO_4 toward electrolyte.

An intriguing part of the present investigation is the role of Mo and Yb, added as impurity in BiVO_4 overlayer, in enhancing the PEC performance of thin-film electrodes. Results suggest that regulated diffusion of impurity cations in BiVO_4 lattice had induced significant alterations in microstructure, particle dimensions, electrical resistivity and film surface roughness that favoured light absorption and reduced recombination losses. Further, TEM analysis indicated part presence of Yb_2O_3 and MoO_3 nanoparticles, being dispersed

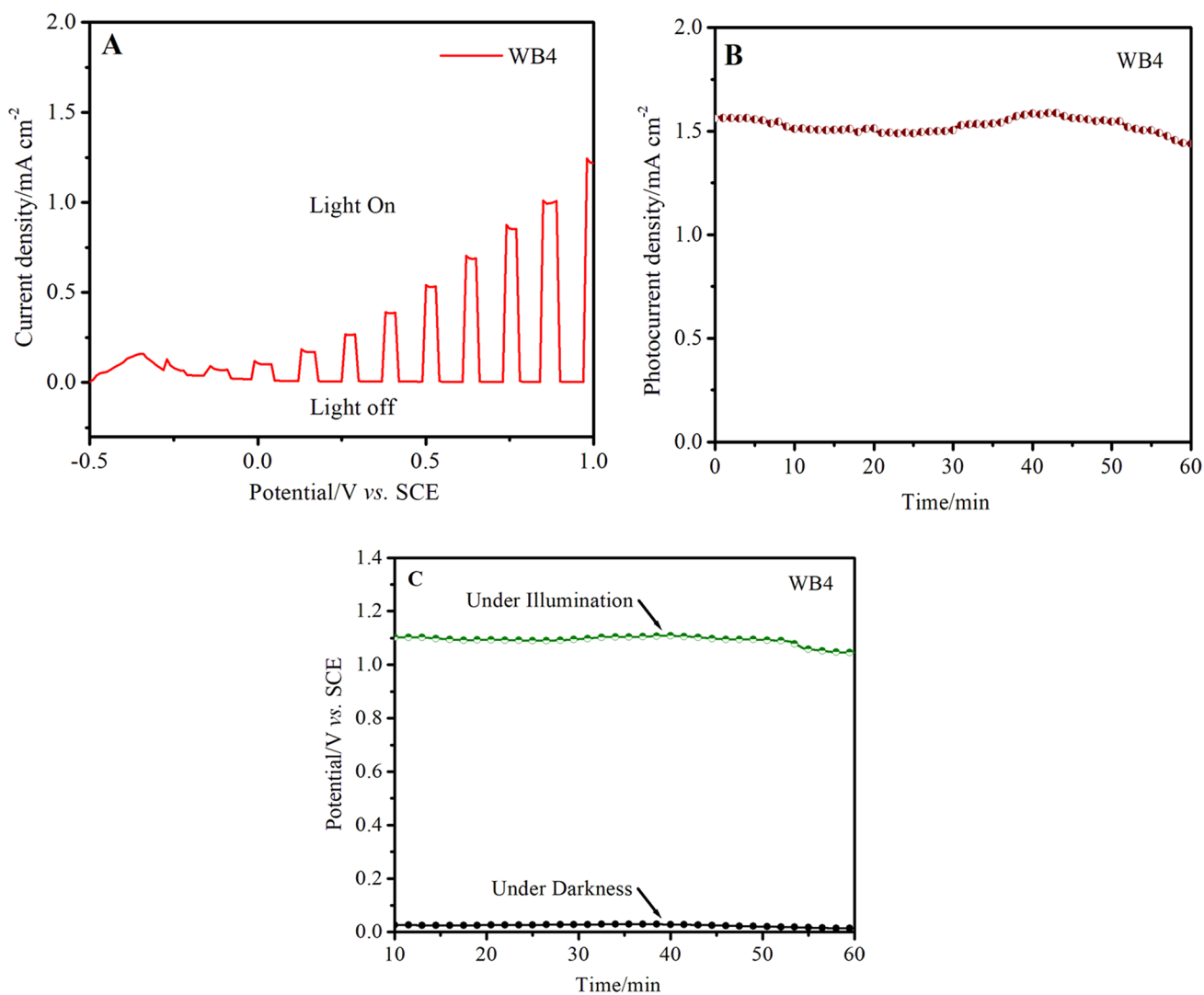


Fig. 13 For sample WB4: I_{ph} measured under chopped illumination (A), extended illumination at 0.8 V vs. SCE (B); $V-t$ plot (C)

in BiVO_4 overlayer. Hence, with their VB lying more negative to the VB of WO_3 and BiVO_4 and more positive to $\text{H}_2\text{O}/\text{O}_2$ redox level, controlled presence of impurity oxides has seemingly also facilitated charge separation and transfer of photogenerated holes from VB of WO_3 and BiVO_4 to electrolyte for oxygen evolution (Fig. 17) [55–57]. Additionally, electrode existing in equilibrium with electrolyte, the surface band bending might have also boosted charge separation, resulting in enhanced photoresponse in the present case.

5 Conclusion

Present study deals with detailed structural and photoelectrochemical investigations on uniquely synthesized BNH thin-film photoelectrodes, $\text{WO}_3/\text{Yb-Mo-BiVO}_4$, for water splitting, against monolayered films of WO_3 , BiVO_4 and Yb-Mo-BiVO_4 . XRD analysis of samples prepared by drop-casting followed by ultrasonic spray deposition on FTO glass substrates reveals the dominant evolution of monoclinic

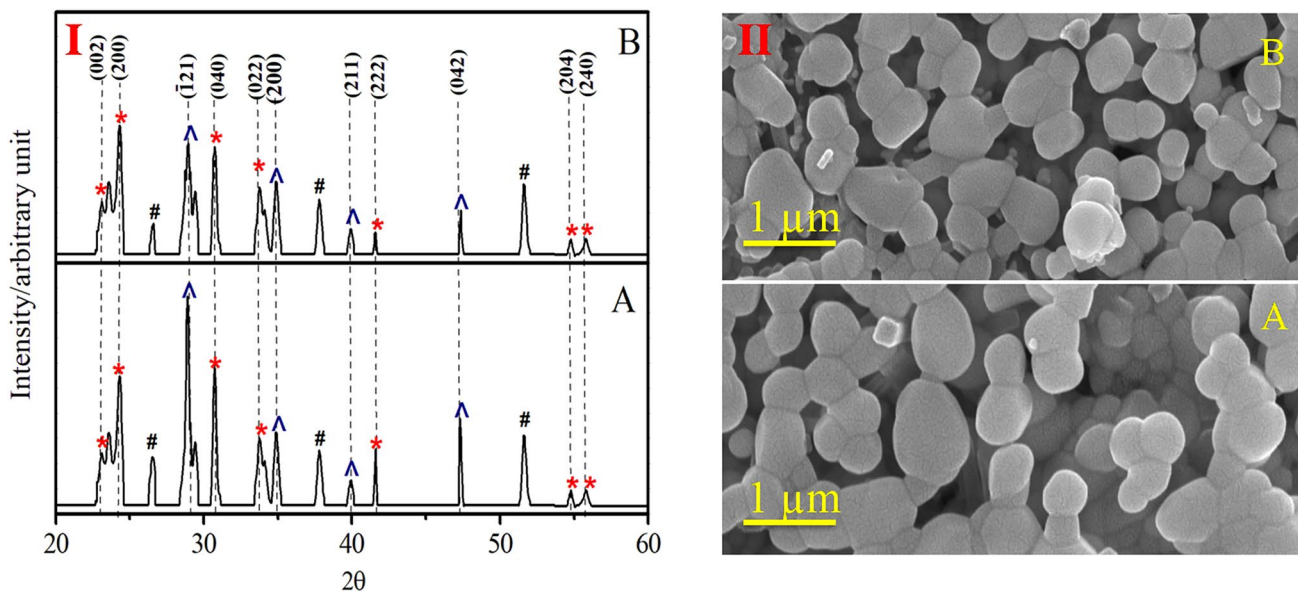


Fig. 14 XRD pattern (I) and SEM images (II) for sample WB4: A – before PEC measurements, B – after 12–15 cycles of PEC measurements

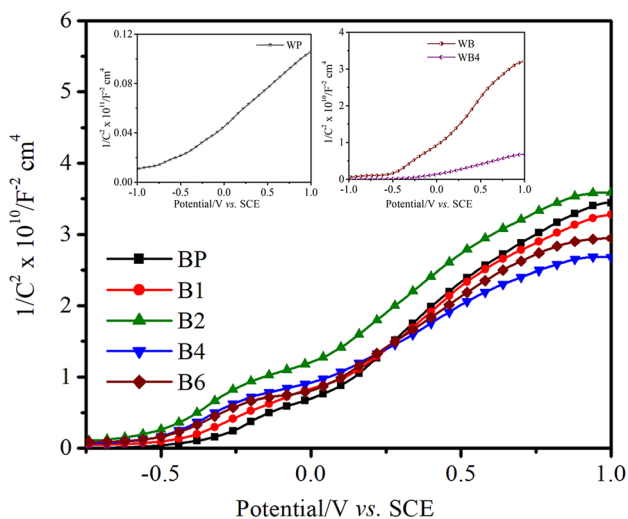


Fig. 15 Mott–Schottky plots for pristine and bilayered thin films

phases of WO_3 and BiVO_4 , with average crystallite size in the range 22–42 nm. Optical analysis shows enhanced and broader absorption of light by BNH films that increases further on Yb–Mo incorporation. BNH films incorporated with 2% at. Mo and 4% at. Yb yielded ~227–950% increase in I_{ph} against monolayered pristine films of WO_3 and BiVO_4 , with I_{ph} rising to 1.67 mA cm^{-2} at 0.85 V vs. SCE. The effect is attributable to significant enhancement in absorption of light, film surface roughness, charge carrier density and reduction in electrical resistivity and recombination losses. Mott–Schottky analysis and Nyquist plots reveal least charge transfer resistance with sample WB4 that yields highest I_{ph} (1.67 mA cm^{-2} at 0.85 V applied potential vs. SCE) and 0.81% ABPE. The study has, thus, clearly established superiority and significance of $\text{WO}_3/\text{Yb-Mo-BiVO}_4$ thin-film photoelectrodes in PEC water splitting.

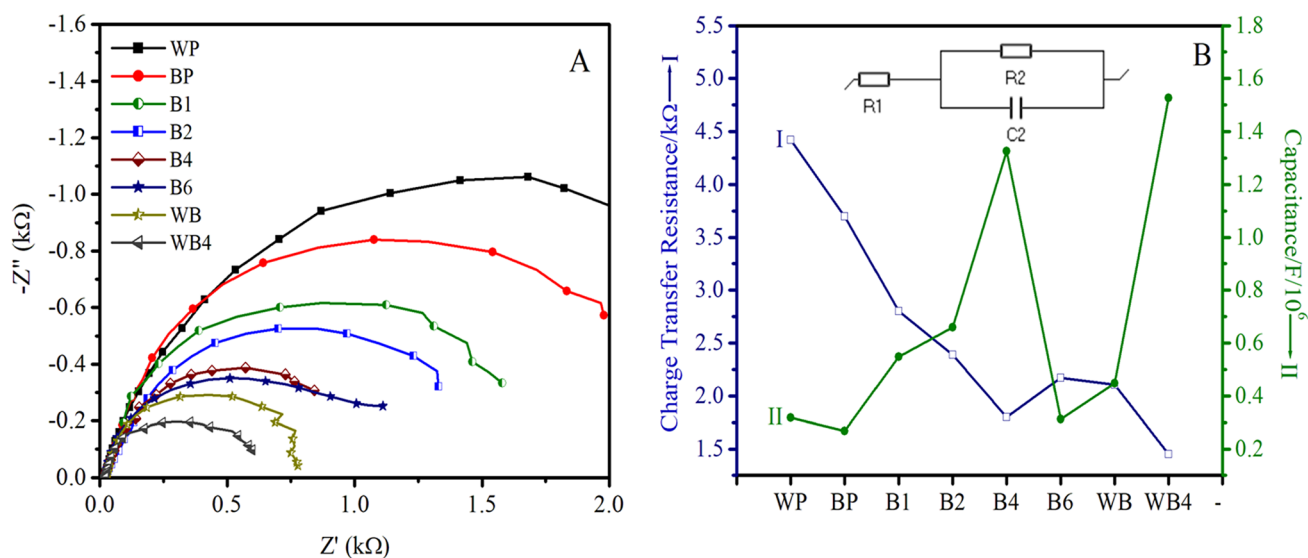


Fig. 16 Nyquist plots for pristine and bilayered thin films

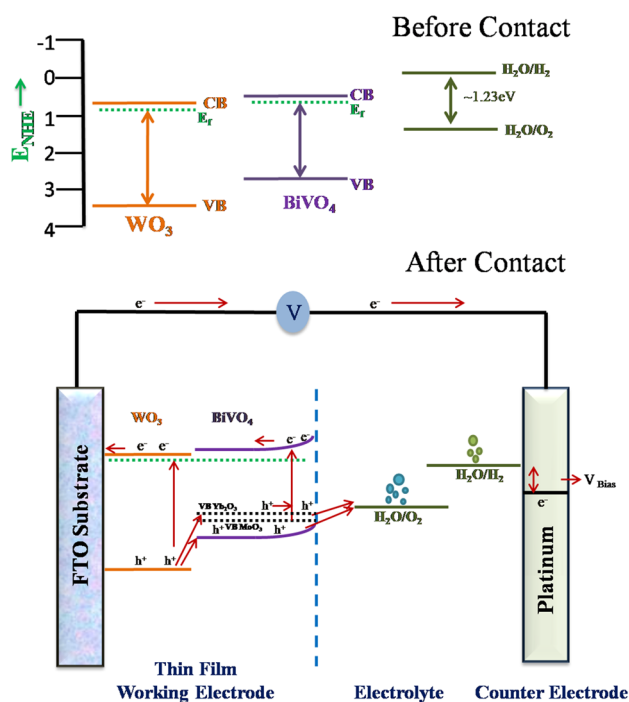


Fig. 17 Tentative mechanism for the movement of photogenerated charge carriers in bilayered films

Acknowledgements This work is financially supported, in parts, by Department of Science and Technology, Ministry of Science and Technology, Government of India (Project Sanction Number: DST/TMD/HFC/2K18/16(C)) and University Grants Commission, Government of India (Project Sanction Number: F. No.194-1/2009(IC)). Authors are

grateful to Prof Prateek Sen, IIT-Kanpur for photoluminescence studies and IIT-Delhi and IIT-Roorkee for XPS and TEM analyses of samples.

References

1. Tee SY, Win KY, Ten WS, Koh LD, Liu S, Teng CP, Han M-Y (2017) Recent progress in energy driven water splitting. *Adv Sci* 4(5):1600337
2. Kaur G, Divya KSA, Satsangi VR, Shrivastav R, Dass S (2021) Nano-hetero-structured thin films, ZnO/Ag-(α)Fe₂O₃, with n/n junction, as efficient photoanode for renewable hydrogen generation via photoelectrochemical water splitting. *Renew Energy* 164:156–170
3. Zou X, Sun Z, Hu HY (2020) g-C₃N₄-based photoelectrodes for photoelectrochemical water splitting: a review. *J Mater Chem A* 8:21474–21502
4. Kaur G, Divya SVR, Dass S, Shrivastav R (2020) 3D-nano-hetero-structured n/n junction, CuO/Ru-ZnO thin films, for hydrogen generation with enhanced photoelectrochemical performances. *Int J Hydrogen Energy* 45:21051–21067
5. Tayebi M, Lee KB (2021) The effects of W/Mo-co-doped BiVO₄ photoanodes for improving photoelectrochemical water splitting performance. *Catalysis* 361:183–190
6. Khoomortezaei S, Hossein A, Golobostanfar RM (2019) Triple layer heterojunction WO₃/BiVO₄/BiFeO₃ porous photoanode for efficient photoelectrochemical water splitting. *Appl Energy Mater* 2:6428–6439
7. Cristino V, Caramori S, Argazzi R, Meda L, Marra LG, Bignozzi LC (2011) Efficient photoelectrochemical water splitting by anodically grown WO₃ electrodes. *Langmuir* 27:7276–7284
8. Zhang K, Shi JX, Kyu Kim J, Hyeok Park J (2012) Photoelectrochemical cells with tungsten trioxide/Mo-doped BiVO₄ bilayers. *Phys Chem Phys* 14:11119–11124
9. Hong SJ, Lee S, Jang SJ, Lee SJ (2011) Heterojunction BiVO₄/WO₃ electrodes for enhanced photoactivity of water oxidation. *Energy Environ Sci* 4:1781–1787

10. Chae YS, Lee SC, Jung H, Joo O, Min KB, Kim HJ, Hwang JY (2017) Insight into charge separation in WO₃/BiVO₄ heterojunction for solar water splitting. *Appl Mater Interfaces* 9:19780–19790
11. Sun Y, Murphy JC, Reyes-Gi RK, Reyes-Gracia AE, Thornton MJ, Morris AN, Raftery D (2009) Photoelectrochemical and structural characterization of carbon-doped WO₃ films prepared via spray pyrolysis. *Int J Hydrogen Energy* 34:8476–8484
12. Prasad U, Prakash J, Gupta KS, Zuniga J, Mao Y, Azeredo B, Kannan MNA (2019) Enhanced photoelectrochemical water splitting with Er and W co-doped bismuth vanadate with WO₃ heterojunction-based two-dimensional photoelectrode. *Appl Mater Interfaces* 11:19029–19039
13. Liu C, Su J, Guo L (2016) Comparison of sandwich and fingers-crossing type WO₃/BiVO₄ multilayer heterojunctions for photoelectrochemical water oxidation. *RSC Adv* 6:27557–27565
14. Grigioni I, Stamplescokie GK, Selli E, Kamat PV (2015) Dynamics of photogenerated charge carriers in WO₃/BiVO₄ heterojunction photoanodes. *J Phys Chem C* 119:20792–20800
15. Lee GM, Kim HD, Sohn W, Moon WC, Park H, Lee S, Jang WH (2016) Conformally coated BiVO₄ nanodots on porosity-controlled WO₃ nanorods as highly efficient type II heterojunction photoanodes for water oxidation. *Nano Energy* 28:250–260
16. Pilli KS, Janarthanan R, Deutsch GT, Furtak ET, Brown DL, Turner AJ, Herring MA (2013) Efficient photoelectrochemical water oxidation over cobalt-phosphate (Co-Pi) catalyst modified BiVO₄/1D-WO₃ heterojunction electrodes. *Phys Chem Chem Phys* 15:14723–1414728
17. Momeni MM, Tahmasebi Z (2021) Effect of electrodeposition time on morphology and photoelectrochemical performance of bismuth vanadate films. *Inorg Chem Commun* 125:108445
18. Huang J, Tan G, Zhang L, Ren H, Xia A, Zhao C (2014) Enhanced photocatalytic activity of tetragonal BiVO₄: Influenced by rare earth ion Yb. *Mater Lett* 133:20–23
19. Su J, Guo L, Bao N, Grimes AC (2011) Nanostructured WO₃/BiVO₄ heterojunction films for efficient photoelectrochemical water splitting. *Nano Lett* 11:1928–1933
20. Xu S, Fu D, Song K, Wang L, Yang Z, Yang W, Hou H (2018) One-dimensional WO₃/BiVO₄ heterojunction photoanodes for efficient photoelectrochemical water splitting. *Chem Eng J* 349:368–375
21. Nozik AJ (1977) Photochemical diodes. *Appl Phys Lett* 30:567–569
22. Momeni MM, Ghayeb Y (2016) Preparation of cobalt coated TiO₂ and WO₃-TiO₂ nanotube films via photo-assisted deposition with enhanced photocatalytic activity under visible light illumination. *Ceram Int* 42:7014–7022
23. Momeni MM, Ghayeb Y, Ezati F (2018) Iron-tungsten/titania nanotube films for photoelectrochemical water splitting. *Surf Eng* 36:6–12
24. Momeni MM, Akbarnia M, Ghayeb Y (2020) Preparation of S-W-codoped TiO₂ nanotubes and effect of various hole scavengers on their photoelectrochemical activity: alcohol series. *Int J Hydrogen Energy* 45:33552–33562
25. Momeni MM, Ghayeb Y, Gheibee S (2017) Silver nanoparticles decorated titanium dioxide-tungsten trioxide nanotube films with enhanced visible light photo catalytic activity. *Ceram Int* 43:564–570
26. Baek HJ, Kim JB, Han SG, Hwang WS, Kim RD, Cho SI, Jung SH (2017) BiVO₄/WO₃/SnO₂ double-hetero-junction photoanode with enhanced charge separation and visible-transparency for bias-free solar water-splitting with a perovskite solar cell. *Appl Mater Interfaces* 9:1479–1487
27. Chatchai P, Murakami Y, Kishioka S, Nosaka AY, Nosaka Y (2009) Efficient photocatalytic activity of water oxidation over WO₃/BiVO₄ composite under visible light irradiation. *Electrochim Acta* 54:1147–1152
28. Serpone N, Borgarello E, Gratzel M (1984) Visible light induced generation of hydrogen from H₂S in mixed semiconductor dispersions; improved efficiency through inter-particle electron transfer. *J Chem Soc Chem Commun* 1476:343–344
29. Momeni MM (2015) Study of synergistic effect among photo-, electro-, and sonoprocesses in photocatalyst degradation of phenol on tungsten-loaded titania nanotubes composite electrode. *Appl Phys A* 119:1413–1422
30. Zhang K, Shi XJ, Kim JK, Park JH (2012) Photoelectrochemical cells with tungsten trioxide/Mo-doped BiVO₄ bilayers. *Phys Chem Chem Phys* 14:11119–11124
31. Prasad U, Prakash J, Kannan A (2020) Effect of yttrium, ytterbium with tungsten co-doping on light absorption and charge transport properties of bismuth vanadate photoanodes to achieve superior photoelectrochemical water splitting. *Sustain Energy Fuels* 4:1496–1506
32. Obregon S, Colon G (2014) Excellent photocatalytic activity of Yb³⁺, Er³⁺ co-doped BiVO₄ photocatalysts. *Appl Catal B* 152:328–334
33. Claudino CH, Kuznetsova M, Rodrigues BS, Chen C, Wang Z, Sardela M, Souza JS (2020) Facile one-pot microwave-assisted synthesis of tungsten-doped BiVO₄/WO₃ heterojunctions with enhanced photocatalytic activity. *Mater Res Bull* 125:110783
34. Kumari B, Sharma S, Singh N, Satsangi VR, Dass S, Shrivastav R (2015) Chemically etched ZnO thin films, with surface evolved nano-ridges, for efficient photoelectrochemical splitting of water. *J Solid State Electrochem* 19:1311–1320
35. Singh S, Chen H, Shahrokhi S, Wang PL, Lin C, Guan X, Tricoli A, Xu JZ, Wu T (2020) Hybrid organic-inorganic materials and composites for photoelectrochemical water splitting. *Energy Lett* 5:1487–1497
36. Sharma S, Pai MR, Kaur G, Divya Satsangi VR, Dass S, Shrivastav R (2019) Efficient hydrogen generation on CuO core/Ag-TiO₂ shell nano-hetero-structures by photocatalytic splitting of water. *Renew Energy* 136:1202–1216
37. Kumari B, Sharma S, Singh N, Verma A, Satsangi VR, Dass S, Shrivastav R (2014) ZnO thin films, surface embedded with biologically derived Ag/Au nanoparticles, for efficient photoelectrochemical splitting of water. *Int J Hydrogen Energy* 39:18216–18229
38. Gupta M, Sharma V, Shrivastava J, Solanki A, Singh AP, Satsangi VR, Das S, Rohit S (2009) Preparation and characterization of nanostructured ZnO thin films for photoelectrochemical splitting of water. *Bull Mater Sci* 32:23–30
39. Banerjee A, Mondal B, Verma A, Satsangi VR, Shrivastav R, Dey A, Dass S (2017) Enhancing efficiency of Fe₂O₃ for robust and proficient solar water splitting using a highly dispersed bioinspired catalyst. *J Catal* 352:83–92
40. Liang Y, Guan ZC, Wang HP, Du RG (2017) Enhanced photoelectrochemical anticorrosion performance of WO₃/TiO₂ nanotube composite films formed by anodization and electrodeposition. *Electrochim Commun* 77:120–123
41. Fujimoto I, Wang N, Saito R, Miseki Y, Gunji T, Sayama K (2014) WO₃/BiVO₄ composite photoelectrode prepared by improved auto-combustion method for highly efficient water splitting. *Int J Hydrogen Energy* 39:2454–2461
42. Shi L, Zhuo S, Abulikemu M, Mettela G, Palaniselvam T, Rasul S, Tang B, Yan B, Saleh NB, Wang P (2018) Annealing temperature effects on photoelectrochemical performance of bismuth vanadate thin film photoelectrodes. *RSC Adv* 8:29179–29188
43. Ding K, Chen B, Fang Z, Zhang Y, Chen Z (2014) Why the photocatalytic activity of Mo-doped BiVO₄ is enhanced: a

- comprehensive density functional study. *Phys Chem Chem Phys* 16:13465–13476
44. Zeng Q, Li L, Bai J, Xia L, Zhou B (2017) Synthesis of WO₃/BiVO₄ photoanode using a reaction of bismuth nitrate with peroxovanadate on WO₃ film for efficient photoelectrocatalytic water splitting and organic pollutant degradation. *Appl Catal B Environ* 217:21–29
 45. Long M, Tan B, Hu P, Zhou B, Zhou Y (2015) Scalable one-step synthesis of TiO₂/WO₃ films on titanium plates with an efficient electron storage ability. *J Mater Chem A* 3:10195–10198
 46. Chatchai P, Murakami Y, Kishioka S, Nosaka AY, Nosaka Y (2009) Efficient photocatalytic activity of water oxidation over WO₃/BiVO₄ composite under visible light irradiation. *Electrochim Acta* 54:1147–1152
 47. Nalajala N, Gopinath SC (2021) Scalable and thin film approach for solar hydrogen generation: a review on enhanced photocatalytic water splitting. *J Mater Chem A* 9:1353–1371
 48. Park Y, McDonald KJ, Choi KS (2013) Progress in bismuth vanadate photoanodes for use in solar water oxidation. *Chem Soc Rev* 42:2321–2337
 49. Sharma V, Kumar P, Shrivastav J, Solanki A, Satsangi VR, Dass S, Shrivastav R (2011) Synthesis and characterization of nanocrystalline Zn_{1-x}M_xO (M = Ni, Cr) thin film for efficient photoelectrochemical splitting of water under UV-irradiation. *Int J Hydrogen Energy* 36:4280–4290
 50. Chatchai P, Kishioka S, Murakami Y, Nosaka AY, Nosaka Y (2010) Enhanced photoelectrocatalytic activity of FTO/WO₃/BiVO₄ electrode modified with gold nanoparticles for water oxidation under visible light irradiation. *Electrochim Acta* 55:592–596
 51. Zhang XL, Wang X, Wang D, Jinhua Y (2019) Conformal BiVO₄-layer/WO₃-nanoplate-array heterojunction photoanode modified with cobalt phosphate co-catalyst for significantly enhanced photoelectrochemical performances. *Appl Mater Interfaces* 11(6):5623–5631
 52. Song J, Huang Z, Pan L, Zou J, Zhang X, Wang L (2015) Oxygen deficient tungsten oxide as versatile and efficient hydrogenation catalyst. *ACS Catal* 5:6594–6599
 53. Grigioni I, Stamplecoskie KG, Jara DH, Dozzi MV, Oriana A, Cerullo G, Kamat PV, Selli E (2017) Wavelength-dependent ultrafast charge carrier separation in the WO₃/BiVO₄ coupled system. *ACS Energy Lett* 2:1362–1367
 54. Shi X, Choi IV, Zhang K, Kwon J, Kim DY, Lee JK, Oh SH, Kim JK (2014) Efficient photoelectrochemical hydrogen production from bismuth vanadate decorated tungsten trioxide helix nanostructures. *Nature Commun* 5:4775–4781
 55. Cho SW, Piper LFJ, DeMasi A, Preston ARH, Smith KE, Chauhan KV, Hatton RA, Jones TS (2010) Soft X-ray spectroscopy of C60/copper phthalocyanine/MoO₃ interfaces: role of reduced MoO₃ on energetic band alignment and improved performance. *J Phys Chem C* 114:18252–18257
 56. Kroger M, Hamwi S, Meyer J, Riedl T, Kowalsky W, Kahn A (2009) p-type doping of organic wide band gap materials by transition metal oxides: a case-study on molybdenum trioxide. *Org Electron* 10:932–938
 57. Julien C, Khelifa A, Hussain OM, Nazri GA (1995) Synthesis and characterization of flash-evaporated MoO₃ thin Films. *J Cryst Growth* 156:235–244

Publisher's Note Springer Nature remains neutral with regard to jurisdictional claims in published maps and institutional affiliations.

Authors and Affiliations

Divya¹ · Jyoti Prakash^{2,3} · Sakshi Saxena¹ · Pushpendra Kumar⁴ · Sahab Dass¹ · Arunachala Mada Kannan² · Rohit Shrivastav¹

¹ Department of Chemistry, Dayalbagh Educational Institute, Dayalbagh, Agra 282005, India

² The Polytechnic School, Ira A. Fulton Schools of Engineering, PRLTA 335A, Arizona State University, 7171 E Sonoran Arroyo Mall, Mesa, AZ 85212, USA

³ Present Address: Materials Group, Bhabha Atomic Research Centre, Trombay, Mumbai 400094, India

⁴ Department of Chemistry, Lovely Professional University, Jalandhar, India